Properties of aerosols and formation mechanisms over southern China during the monsoon season

Weihua Chen[1], Xuemei Wang[2]*, Jason Blake Cohen[2], Shengzhen Zhou[2*],

Zhisheng Zhang[3], Ming Chang[1], and Chuen Yu Chan[4]

[1]*School of Environmental Science and Engineering, Sun Yat-Sen University, Guangzhou, China*

[2]*School of Atmospheric Sciences, Sun Yat-Sen University, Guangzhou, China*

[3]*South China Institute of Environmental Sciences, Guangzhou, China*

[4]*Key Laboratory of Aerosol, SKLLQG, Institute of Earth Environment, Chinese Academy of Sciences, Xi'an, China*

*Corresponding author:
Xuemei Wang (eeswxm@mail.sysu.edu.cn)
Shengzhen Zhou (zhoushzh3@mail.sysu.edu.cn)

Abstract

Measurements of size-resolved aerosols from 0.25 to 18 μm were conducted at three sites (urban, suburban and background sites) and used in tandem with an atmospheric transport model to study the size distribution and formation of atmospheric aerosols in southern China during the monsoon season (May-June) in 2010. The mass distribution showed the majority of chemical components were found in the smaller size bins (<2.5 μm). Sulfate, was found to be strongly correlated with aerosol water, and anti-correlated with atmospheric SO_2, hinting at aqueous-phase reactions being the main formation pathway. Nitrate was the only major species that showed a bi-modal distribution at the urban site, and was dominated by the coarse mode in the other two sites, suggesting that an important component of nitrate formation is chloride depletion of sea salt transported from the South China Sea. In addition to these aqueous-phase reactions and interactions with sea salt aerosols, new particle formation, chemical aging, and long-range transport from upwind urban or biomass burning regions were also found to be important in at least some of the sights on some of the days. This work therefore summarizes the different mechanisms that significantly impact the aerosol chemical composition during the Monsoon over southern China.

Keywords: chemical component, mass size distribution, aqueous-phase reaction chloride depletion

1. Introduction

Atmospheric aerosols are solid and liquid substances ubiquitously suspended in the Earth's atmosphere, that impair visibility, negatively affect human health, and directly and indirectly impact regional and global climate (Burnett et al., 2014; Chen et al., 2013a; Chung and Seinfeld, 2005; Cohen et al., 2011; Huang et al., 2014; Jacobson, 2001; Kim et al., 2008; Liu et al., 2011; Ramanathan and Carmichael, 2008; Rosenfeld et al., 2014; Tao et al., 2009). The size distributions and chemical composition of aerosols play essential roles on their transport, transformation, removal mechanisms (Cohen and Prinn, 2011; Cohen and Wang, 2013; Delene and Ogren, 2002; Dubovik et al., 2000; Giglio et al., 2003, 2006; Petrenko, et al., 2012; Seinfeld and Pandis, 2006; Zhao and Gao, 2008a). And also, to some extent, they provide useful information to validate and improve model performance (Cohen and Wang, 2013; Cohen, 2014; Cohen and Lecoeur, 2015; Myhre et al., 2013; Pillai and Moorthy, 2001; Schuster et al., 2006; Tsigaridis et al., 2014). In the environment, the most important aerosol processes occur over the Aitken (<0.1 μm), condensation (~0.1-0.5 μm), droplet (~0.5-2.0 μm), and coarse (>2.0 μm) size modes (Seinfeld and Pandis, 2006), where new particles are formed in the Aitken mode via condensational growth and coagulation of nucleation mode particles, and droplet mode particles are produced by in-cloud processing or aqueous reactions (Ervens et al., 2011; Lim et al., 2010; Meng and Seinfeld, 1994; Volkamer et al., 2009; Wang et al., 2012; Yao et al, 2003a). On the other hand, coarse mode aerosols usually come from very different sources than smaller aerosols. For example, natural sources such as sea spray, dust,

67   soil, and active biological aerosols are unique and therefore provide further

68   information about the aerosol distribution at a given location.

69   Previous research suggests that sulfate is mostly contained in the non-coarse

70   modes, with the conversion of SO_2 occurring mostly via gas-phase oxidation followed

71   by condensation, or through droplet mode sulfate produced from fog/cloud process

72   (Barth et al., 1992; Meng and Seinfeld, 1994). On the other hand, nitrate usually has a

73   bi-modal distribution with peaks in both the fine and coarse modes. Fine mode nitrate

74   is formed mainly by oxidation of NO_2 to HNO_3 and subsequent condensation, or from

75   the heterogeneous hydrolysis of N_2O_5, while coarse mode nitrate is often observed

76   due to the effect of chloride depletion of sea salt aerosols (Harrison and Pio, 1983;

77   Pierson and Brachaczek, 1998). Ammonium is mostly found in the fine mode and is

78   chemically associated with sulfate and nitrate. Carbonaceous materials, organic

79   carbon (OC) and elemental carbon (EC), are both found primarily in the non-coarse

80   mode. While both OC and EC are impacted by differing emissions sources and wet

81   deposition, there are other significant differences: EC is hydrophobic and radiatively

82   active, while OC is hydrophylic and further has significant source terms from

83   condensation and secondary particle formation (Lan et al., 2011).

84   A series of studies about the mass size distribution of aerosol chemical

85   components have conducted at a specific site over Southern China during the past

86   decade (Lan et al., 2011; Liu et al., 2008; Yang and Wenig, 2009; Zhang et al., 2015).

87   Compared with the previous studies, this paper presents a unique combination of

88   analytical and measurement techniques. We use measurements of chemical properties

89   and size distribution conducted at three different functional sites, coupled with

90   multiple modeling results, and reprocess remote sensing products using statistical

91   methods, all in tandem with each other, which is not commonly found in other studies.

92   Furthermore, we test our approach in Southern China, which is one of the regions of

93   the world with the most complex meteorology, coming under the influence of the

94   Monsoon, with shifting winds from continental and oceanic sources. Additionally, the

95   season tested is a transition period, during which there were significant

96   meteorological contributions from both remote continental sources as well as oceanic

97   sources. On top of this, Southern China has a combination of high temperature and

98   relative humidity, strong radiative flux, and high oxidative capacity, leading to the

99   promotion of significant secondary aerosol formation.

100   In this paper, we present a unique database of the size-different mass distribution

101   of aerosol chemical components during the Monsoon Season over southern China.

102   The data were sampled from a combination of three different sites, one in an urban

103   area, one in a suburban area, and one in a remote area, providing further insights into

104   the characteristics of size distribution in each of these regions, and discussion on the

105   secondary aerosol formation mechanisms, the identification and impacts of

106   long-range transport of biomass and urban sources, and the impacts of mixing sea-salt

107   and urban pollutants on the characteristics of aerosol size distribution.

108

109   **2. Measurements and methodology**

110   **2.1. Description of the sampling sites**

111   The field study was conducted at three sites in southern China (Figure 1), two of

112   which were situated in Guangdong and the other in Hainan. Guangdong is located in a

113   subtropical monsoon climate, primarily influenced by cold and dry air masses from

114   the North in December to February, and warm and wet air masses from the South

115   China Sea in May to August. It has a single annual local rainy season extending from

116   April to September. Hainan is located further to the south, and has year-round warm

117   to hot weather and a distinct rainy season from May to October.

118   The first site (23.12°N, 113.36°E), is located on the rooftop of a building in the

119   South China Institute of Environmental Sciences, Guangzhou (GZ), a mega-city

120   containing more than 13 million people. The site was located about 50m above

121   ground, in an area surrounded by residential and commercial buildings, with the

122   nearest arterial roads located about 200m away. There were no significant industrial

123   emission sources found around the site. This site was chosen since it is highly

124   representative of a typical megacity.

125   The second site was located at (22.34°N, 113.58°E), on the rooftop of the library

126   at Sun Yat-Sen University, in the city of Zhuhai (ZH), a medium sized city of about

127   1.6 million people located in Southern Guangdong adjacent to Macau. The site was

128   located about 60m above the ground, in an area surrounded by mountains on three

129   sides and the estuary where the Pearl River meets the South China Sea about 500m

130   away on the fourth side. There are no significant industrial or major transportation

131   emissions sources nearby. This site was chosen since it is highly representative of a

132   coastal partially urbanized area.

133   The third site was located at Jianfeng Mountain (JFM, 18.74°N, 108.86°E), in a

134   tropical rainforest situated in the Southwest corner of Hainan. This site is distant from

135   the major cities of Hainan province and is further located about 5km away from the

136   coast. JFM is not directly influenced by anthropogenic emissions and is generally

137   regarded as a background site to investigate the long-range transport (Zhang et al.,

138   2013a). This site was chosen both because it is representative of a remote site and

139   because it receives air masses from three different directions: continental East Asia to

140   the North, the South China Sea to the South, and Southeast Asia to the West.

141

142   **2.2 Sampling of aerosol**

143   To attain size-segregated particle samples, a 6-stage High Flow Impactor (MSP)

144   with an airflow rate of 100 L min^{-1} was employed, with cutoff diameters (D_p) of 18

145   (inlet), 10, 2.5, 1.4, 1.0, 0.44 and 0.25 μm. A total of 10, 8 and 20 sets of

146   size-segregated particle samples were collected in GZ, ZH and JFM, respectively

147   during the periods of May and June in 2010 (shown in Figure 2). A single set of

148   sample collection lasted for approximately 24h in GZ and ZH, and 48h in JFM. Since

149   the aerosol concentration was relatively low in remote JFM site, we extended the

150   sampling time as long as 48h to allow the chemical components to be detected.

151   The mass concentrations of six cations (Na^+, NH_4^+, K^+, Ca^{2+}, Mg^{2+}, and Ca^{2+}) and

152   seven anions (F^-, Cl^-, NO_2^-, Br^-, SO_4^{2-}, NO_3^- and PO_4^-) were analyzed using an ion

153   chromatography (ICS-3000, DIONEX). Thermal Optical Transmittance (TOT)

154   technique was employed to analyze the quartz filter samples to determine the mass

155   concentrations of organic carbon (OC) and elemental carbon (EC) by the use of

156   Sunset Laboratory OCEC Carbon Aerosol Analyzer. Detailed information of the

157   aerosol sampling and in-lab chemical analytical techniques can be found in Zhang et

158   al. (2013a).

159   To be consistent with the background literature (4 modes include Aitken (<0.1

160   μm), condensation (~0.1-0.5 μm), droplet (~0.5-2.0 μm), and coarse (>2.0 μm))

161   (Seinfeld and Pandis, 2006), and the constraints of the size bins measured in this study,

162   we implement 2.5 μm as the cut-off size to separate fine and coarse particles, and the

163   size bins from 0.44-1.4 μm was defined as droplet particles in this study. Although we

164   were not able to directly measure aerosol water content, given its importance for the

165   study here, we instead estimate the amount by the use of E-AIM model II (Clegg et al.,

166   1998), as it provides the most accurate prediction compared with other models, like

167   ISORROPIA and SCAPE2 (Yao et al., 2006). The input parameters of the E-AIM

168   model II are tempreture, relative humidity, strong acidity (H^+), molar contentrations of

169   NH_4^+, SO_4^{2-} and NO_3^- ions (Clegg et al., 1998). Further, an approximation of the

170   particle strong acidity $[H^+]_s$ was calculated using Eq. (1):

171    $$\left[H^+ \right]_s = 2\left[SO4^{2-} \right] + \left[NO_3^- \right] - \left[NH_4^+ \right] \qquad (1)$$

172   The calculation of strong acidity would introduce possible errors due to the

173   exclusion of other ions (e.g. K^+, Na^+, Cl^-), but which only exerted a minor influence

174   on the estimation of aerosol acidity due to their lower concentration (Yao et al., 2006).

175   **2.3 Meteorological data**

176   Meteorological parameters, including wind speed (WS), wind direction (WD),

177   temperature (T), relative humidity (RH), pressure (P), and precipitation were

178   simultaneously monitored in GZ and JFM sites with a time resolution of 30 minutes.

179   The same meteorological parameters in ZH, as well as the daily low-level cloud cover

180   data at all three sites, were obtained from the China Meteorological Data Sharing

181   Service System (http://data.cma.cn/site/index.html).

182

183   **2.4 Remotely sensed measurements**

184   Aerosol optical depth (AOD), fire products including Fire Radiative Power (FRP),

185   and Fire Quality Assurance [QA] data, were obtained from the MODIS sensors

186   aboard both the AQUA and TERRA satellites. Specifically, we obtained the

187   Collection 6, 3km Level 2 swath product for AOD (Remer et al., 2013), and

188   Collection 5.1, 1km Level 2 swath products for FRP and QA (Giglio et al., 2006). The

189   Collection 5.1 active fire products are daily products and have been improved based

190   on the previous collection 5.0 products. All of the data are cloud-screened, with AOD

191   data being computed using different algorithms over land and water, and the fire data

192   using 19 different channels for quality assurance. We only accept values for FRP and

193   Fire Count where the QA is at least 90%.

194

195   **2.5 Atmospheric transport model**

196   Two Lagrangian particle dispersion models, the Hybrid Single Particle Lagrangian

197   Integrated Trajectory (HYSPLIT) (Draxler and Hes, 1998) and FLEXPART coupled

198   with The Weather and Research and Forecasting (WRF) model (FLEXPART –WRF)

199 (Stohl et al., 1998; Brioude et al., 2013) were applied to determine the origin of air

200 masses in this study, Compared with HYSPLIT, FLEXPART can identify the relative

201 importance of source region that affected the receptor visually. HYSPLIT uses single

202 air parcels to compute trajectories with the use of Global Data Assimilation System

203 (GDAS, $1°×1°$) as input data. FLEXPART, on the other hand, uses a larger number of

204 air parcels to compute trajectories based on the higher resolution meteorological

205 predictions provided by mesoscale model WRF. The application of FLEXPART –

206 WRF with a novel convective scheme being added improves the dispersion

207 simulations and results in an overall better simulation, especially for finer scale

208 applications (Brioude et al., 2013; Stohl, 1998). In this case, the region was modeled

209 with a spatial resolution of $27×27$ km and a temporal resolution of 1 hour.

210 An Eulerian model, WRF/Chem V3.4.1 was used in this study to simulate the fog

211 process. For this model, the target region was modeled at a spatial resolution of

212 $3×3km$ and a temporal resolution of 1 hour. Detail information about the WRF/Chem

213 model set-up refers to Situ et al. (2013).

214

215 **3. Results and discussion**

216 **3.1. Overall aerosol characteristics**

217 The time series of PM_{18} chemical compositions at the three sites during the

218 sampling period were shown in Figure 2. The average concentration and standard

219 deviation of PM_{18} was 47.8±20.8, 24.3±12.1 and 8.1±2.7 μg m^{-3} in GZ, ZH and JFM,

220 respectively. The mean and range of PM_{18} in highly urban GZ was both higher and

221 wider than in suburban ZH and rural JFM, with the respective ranges being 23.3~93.7,

222 13.3~35.1, 4.7~14.3μg m^{-3} in the three sites. Maximum concentration was found both

223 on 12th Jun. in GZ and ZH, while it was on 3rd Jun. in JFM (to be discussed later).

224 Table 1 listed the average concentration of chemical components in the given

225 size-resolved particle (PM$_{1.0}$, PM$_{2.5}$ and PM$_{10}$) and their percentage of PM$_{10}$ at the

226 three sites. In terms of the mass size distribution, the percentage of PM$_{1.0}$ to PM$_{10}$ was

227 60.2%, 66.3% and 75.0%, and PM$_{2.5}$ to PM$_{10}$ was 88.0%, 92.6%, 91.7% in GZ, ZH

228 and JFM, respectively. When considered as a whole, it is the smaller sized particles

229 that dominate the aerosol loading at all three of these sites. Looking at the data on a

230 species-by-species level, most of chemical components were concentrated in fine

231 mode particles, which contribute at least 57% to PM$_{2.5}$. The sole exception is nitrate at

232 ZH and JFM, which were mainly concentrated in the coarse mode with a percentage

233 of above 90%. Overall, the sum of five major chemical components (i.e. sulfate,

234 nitrate, ammonium, OC, and EC) accounted for about 90% of the total mass

235 concentration of detected chemical components across all three sites.

236 Two of the species, sulfate and OC, were found to dominate the particle

237 composition, with concentration of 11.7 ± 5.2, 8.8 ± 3.2, 2.2 ± 1.5 μg m^{-3} for sulfate

238 and 7.2 ± 2.7, 3.0 ± 1.5, 1.8 ± 0.8 μg m^{-3} for OC in GZ, ZH and JFM, respectively.

239 Sulfate concentration was much higher than that of OC in urban and suburban

240 locations irrespective of particle size, while OC concentration was similar to that of

241 sulfate in fine particles and slightly higher in coarse particles at the remote site. These

242 findings are consistent with the nature of the sources of sulfur from industrial and

243 power plant (Zheng et al., 2009). In addition, shipping source was becoming

244 increasingly vital for SO_2 emission with an increment of 12% per year in this region

245 (Lu et al., 2013; Zhou et al, 2016)

246   Nitrate, mainly formed from the oxidation of NOx emitted by mobile vehicles

247 and power plants, showed a remarkable difference between urban and background site,

248 ranging from fourteen to thirty times higher in GZ than in the other sites, especially

249 for fine mode nitrate. This is consistent with its more rapid oxidation of its abundant

250 precursor species, especially so in the urban atmosphere (Cohen et al., 2011). In

251 addition, phase equilibrium was another important reason for the discrepancy in urban

252 and background site since nitrate would tend to exist as gas phase while transported to

253 background areas (Seinfeld and Pandis, 2006). A relatively insignificant concentration

254 of NO_3^- in ZH and JFM indicated far less anthropogenic emission of the precursor

255 over these two sites.

256   The values of OC and EC in $PM_{2.5}$ were 7.2 ± 2.7 and 3.4 ± 3.2 $\mu g\ m^{-3}$ in GZ,

257 3.0 ± 1.5 and 1.5 ± 0.9 $\mu g\ m^{-3}$ in ZH. These values were lower than that found in

258 previous studies done in GZ and ZH during the wet season: OC and EC were 13.1 and

259 $4.6\ \mu g \cdot m^3$ in GZ in 2007, 14.8 and 8.1 $\mu g\ m^{-3}$ in GZ in 2002, and 5.4 and 1.9 $\mu g\ m^{-3}$ in

260 ZH in 2002 (Cao et al., 2004; Tao et al., 2009). Furthermore, OC and EC

261 concentrations in JFM were found to be lower than that at other forest sites in China,

262 such as Hengshan: 3.01 and 0.54 $\mu g\ m^{-3}$ in 2009 (Zhou et al., 2012), Daihai: 8.1 and

263 1.81 $\mu g\ m^{-3}$ in 2007 (Han et al., 2008), and Taishan: 6.07 and 1.77 $\mu g\ m^{-3}$ in 2007

264 (Wang et al., 2011). However, the EC and OC in JFM were similar to some

265 background sites in other countries, such as Puy De Dome in France: 2.4 and 0.26 μg

266 m^{-3} in 2004 (Pio et al., 2007) and Sonnblick in Austria: 1.38 and 0.23 μg m^{-3} in 2003

267 (Pio et al., 2007). This finding is not unexpected, since there are very few urban

268 sources near the site. It is therefore relatively representative of a remote background

269 site, and will be treated as such subsequently in this paper.

270

271 **3.2. Size distribution by chemical composition**

272 The mass size distribution of major compositions at the three sites during the

273 study period, shows that sulfate had a single-peaked distribution, with the maximum

274 value found in the 0.44-1.0 μm size over all sites and under all different

275 meteorological conditions examined in this study. The droplet mode sulfate was about

276 56.0 ± 8.0 %, 63.5 ± 5.1 % and 58.8 ± 9.4 % of the total sulfate mass in GZ, ZH and

277 JFM, respectively (Figure 3). This confirms that secondary processing is essential,

278 with aqueous-phase reactions playing a crucial role on the formation and/or growth of

279 droplet sulfate, throughout all of these different regions. It is interesting to note that

280 ZH had the highest relative concentration of droplet model sulfate, which although it

281 is less urban than GZ, is consistent with the fact that it is located very close to large

282 amounts of sulfur emissions from the shipping traffic at the massive nearby ports of

283 Hong Kong and Shenzhen (Lu et al., 2013).

284 Droplet mode ammonium was mainly due to ammonia vapor that reacted with or

285 condensed on an acidic particle surface. Ammonia was observed to highly correlate

286 with sulfate at the three sites (R>0.81, P<0.01), particularly so in the size range of

13

287 0.44-1.0 μm. This is consistent with the fact that sulfuric acid preferentially reacts

288 with ammonia (Zhuang et al., 1999), and that most of sulfate in the atmosphere is

289 generally found as ammonium sulfate in the droplet mode (Liu et al., 2008; Zhuang et

290 al., 1999).

291   The nitrate size distribution was found to be bi-modal in GZ, with the peaks

292 occurring in the 0.44-1.0 μm and 2.5-10 μm size ranges. This is consistent with the

293 fact that Droplet mode nitrate was dominated by the heterogeneous aqueous reaction

294 of gaseous nitric acid (HNO_3) and ammonia (NH_3) on the wet surfaces of pre-existing

295 aerosols within ammonia-rich environment, otherwise by heterogeneous hydrolysis of

296 N_2O_5 on the pre-existing aerosols within ammonia-poor conditions. The dissociation

297 equilibrium of NH_4NO_3 highly depends on temperature and humidity (Stelson and

298 Seinfeld, 1982). On the other hand, this result is consistent with the fact that nitrate

299 was found mostly in the coarse mode in ZH and JFM, where it accounted for up to 60%

300 of total particulate mass. A higher relative humidity, consistent with the warm and wet

301 atmosphere over the South China Sea, makes gaseous nitric acid more likely to be

302 absorbed by coarse particles in the atmosphere (Anlauf et al., 2006), resulting in a

303 higher relative concentration of nitrate in the coarse mode in ZH and JFM (where the

304 relative humidity averaged 80 and 91% respectively, as compared to only 73% in GZ).

305 Further, the presence of coarse mode nitrate is consistent with chlorine reduction, as

306 talked about later.

307   OC and EC showed a similar mono-modal distribution in GZ and ZH, with a

308 dominant and a broad peak over the range from 0.25-1.4 μm. On the other hand, a

309 bi-modal distribution was found in JFM. In urban and suburban areas, there are

310 significant primary sources from traffic and industry in the e.g. Huang et al. (2006)

311 and Cao et al. (2004). It is also consistent with the high-level emissions due to the

312 ship traffic to Shenzhen and Hong Kong, both of which are located near ZH, which in

313 turn would compensate for the otherwise reduced industrial and traffic sources (Zheng

314 et al., 2012). OC has both primary sources, which are similar to those for EC as well

315 as secondary formation. There were a few days in which the ratios of OC to EC are

316 not consistent, indicating a large secondary source of OC. We investigated these days

317 and find that emissions that long-range transported from far-upwind areas with highly

318 urbanization or with the existence of biomass burning are responsible, as discussed

319 later in this paper. Additionally, there is some coarse mode OC present in JFM,

320 suggesting a possible source of biological aerosol (e.g. pollen, spores and plant

321 fragment) (Heald and Spracklen, 2009; Seinfeld and Pandis, 2006; Zhang et al., 2015),

322 which is consistent with the large amounts of vegetation present in that region (Zhang

323 et al., 2015).

324

325 **3.3. Observed Aqueous-phase reaction of droplet mode sulfate**

326 The daily droplet mode sulfate ranged from 3.0-13.6, 1.6-9.5 and 0.5-4.9 $\mu g \ m^{-3}$

327 in GZ, ZH and JFM respectively. In order to study the aqueous-phase reaction of

328 droplet mode sulfate, cases with the air masses came from continent were excluded to

329 avoid the effect of transported pollutants on the concentration of sulfate. Then two

330 cases with a concentration of droplet sulfate above the mean plus one standard

331   deviation were selected as typical cases in each site (8th and 12th May in GZ, 12th May

332   and 1st Jun. in ZH, and 4th and 13th May 2010 in JFM), which were more obvious to

333   observe to investigate the effect of aqueous-phase reaction in the formation of droplet

334   mode sulfate (blue shade in Figure 2). In each of these cases, it was found that droplet

335   mode sulfate accounted for about two thirds of the total mass concentration of sulfate

336   at the three sites.

337   A backward trajectory analysis found that during these events, the air masses at

338   these sites mainly originated over the South China Sea (figures not shown here).

339   Additionally, it was determined that during these times at the three sites, there was an

340   abnormally high amount of low cloud cover 60-70% and a relatively higher relative

341   humidity (75~83%) (Table 2). This combination is consistent with moist air being

342   transported over land where the ship and industrial SO_2 emissions can undergo

343   chemistry in the presence of large amounts of liquid cloud water, to form

344   droplet-model sulfate.

345   We estimated the liquid water content using the AIM-II model (Equation 1). The

346   results showed a significant positive correlation with droplet mode sulfate in GZ

347   (R=0.98, P<0.05), ZH (R=0.53, P<0.05) and JFM (R=0.80, P<0.05), indicating that

348   water content correlated closely with the sulfate aerosol loadings. This is further

349   evidenced that aqueous formation was likely an important contributing factor.

350   We further investigated the aqueous-phase reaction of particles due to the fog

351   process for the data from 8th May in GZ. This is because the measured visibility met

352   the World Meteorological Organization cutoff value of less than 1 km due to water

353 droplets, in the early morning (05:00-07:00 LT) (Figure 4(c)). Consistently, during

354 this time, it was found that the relative humidity was quite high (RH>90%) and the

355 wind was quite low (wind speeds<1.0 m s^{-1}). Also during this time, the cloud fraction

356 and simulated 2m relative humidity were up to 90% over Southern China (Figure

357 4(a-b)). Furthermore, the depression dew point (ΔT=T-Td, while Td denotes dew

358 point temperature) was lower than 1 (Figure 4(c)), which indicating that vapor

359 pressure was saturated. An accompanying analysis using WRF/Chem shows that

360 simulated cloud water mixing ratio was the highest during this period over the GZ

361 area and higher value was found around 06:00 LT (Figure 4(e-f)). This combination

362 promoted the existence of fog/low cloud.

363 Further analysis was done by looking at measurements of SO$_2$ (data from

364 Guangzhou Environmental Protection Bureau, http://www.gzepb.gov.cn/). The

365 diurnal variation on 8th May showed a unique pattern compared with the mean diurnal

366 pattern as measured during 2009-2011 (Figure 4(d)). On this day, the SO$_2$

367 concentration has decreased dramatically since 05:00-07:00 LT, which is consistent

368 with SO$_2$ transferred from the gas to aqueous phase due to the high solubility of SO$_2$

369 in fog water droplets (Zhang et al., 2013b).

370 Simulation of these conditions using WRF/Chem indicates that the rapid growth

371 of both Aitken and accumulation (~0.1-1 μm) mode sulfate started at 07:00 LT and

372 peaked at 08:00-09:00 LT (Figure 4(g-h)). This further supports the conclusion of

373 fresh sulfate production, in this case through both the aqueous and potential initial gas

374 to particle formation, followed by condensation/coagulation and uptake into the liquid

375 droplets present. All of this is consistent with generalized urban modeling studies

376 performed under similar conditions (e.g. Cohen and Prinn, 2011).

377

378 **3.4. Observed interactions between nitrate and chloride depletion**

379   The mass size distribution of Cl^- and Na^+ showed a similar pattern to nitrate at the

380 three sites, peaking in coarse mode particles (Figure 5(a-c)) with an average

381 percentage of 43%, 62% and 43% for coarse mode Na^+, 53%, 76% and 74% for

382 coarse mode Cl^- in GZ, ZH and JFM, respectively, suggesting the main sea salt

383 sources. Na^+ and Cl^- shown a bi-modal distribution in GZ, illustrating the combustion

384 emissions, e.g. biomass burning or coal combustion for fine mode Na^+ and Cl^- (Wang

385 et al., 2005), but the contributions were insignificant since the magnitude of Na^+ and

386 Cl^- from combustion sources is many orders of magnitude smaller than oceanic

387 sources. Furthermore, if the biomass burning source were significant, it would clearly

388 also show up in terms of the K^+ and BC/OC ratio, as explained later in the section *3.6*

389 *Quantifying the impacts of fires*.

390   The concentration and percentage of chloride depletion ($[Cl_{dep}]$ and $\%Cl_{dep}$)

391 were calculated using Eq. (2-3), where $[Cl_{meas}^-]$ and $[Na_{meas}^+]$ are the measured molar

392 concentrations of chloride and sodium respectively, 1.174 was the molar ratio of Cl^- to

393 Na^+ in sea water (Yao et al., 2003b).

394 $$[Cl_{dep}]=1.174[Na_{meas}^+]-[Cl_{meas}] \tag{2}$$

395 $$\%Cl_{dep}=\frac{1.174[Na_{meas}^+]-[Cl_{meas}]}{1.174[Na_{meas}^+]}*100\% \tag{3}$$

396   The positive value of $[Cl_{dep}]$ represents chloride depletion, otherwise means the

397 chloride enrichment, suggesting additional sources was existed for Cl⁻ excluding sea

398 salt. Therefore, samples with negative $[Cl_{dep}]$ were excluded from analysis to avoid

399 the effect of non-sea salt emission on chloride depletion.

400   In general, the %Cl$_{dep}$ decreased as the aerosol mass increased (Figure 5(d)).

401 Chloride had been almost entirely depleted in fine mode particles with the value of

402 91%, while the value was 60% in coarse mode particles in ZH and JFM. The chloride

403 depletion was relatively weaker in GZ with a value of 72% and 47% in fine and

404 coarse mode particle, which was in consistent with that the urban area was less

405 affected by ocean emission. The result was consistent with a study conducted in South

406 China Sea in 2004 as well as the theory that reaction between sulfuric acid and nitric

407 acid with sea salt (sodium chloride) is facilitated in fine particles due to their larger

408 surface areas to volume ratio and longer atmospheric residence time (Chatterjee et al.,

409 2010; Hsu et al., 2007).

410   The ratio of calculated ammonium to measured ammonium was used to explain

411 the presence of sulfuric acid and nitric acid in the aerosol, with a value larger than 1

412 indicating there was insufficient ammonium to neutralize nitric acidic NO_3^- (since

413 ammonium first consumes sulfuric acid). Calculated ammonium was equal to

414 2*[nss-SO_4^{2-}]+[NO_3^-], where[nss-SO_4^{2-}] and [NO_3^-] reprents the molar concentarion

415 of non-sea-salt SO_4^{2-} (i.e., [nss-SO_4^{2-}]=[SO_4^{2-}]−0.14×[Cl^-]) and NO_3^- (Huang et al.,

416 2004). The calculated ratio was much higher than 1 in ZH and JFM suggesting that

417 nitrate plays a role in Cl depletion. The ratio of nitrate to percent chloride depletion

418 can then be used to calculate the contribution of coarse nitrate to chloride depletion

19

419 (Zhuang et al., 1999; Zhao and Gao, 2008b). This result showed that nitrate was

420 responsible for the depletion of 54% and 17% of coarse chloride in ZH and JFM

421 respectively. This suggests that the interaction of sea salt particles with anthropogenic

422 pollutants is an important pathway for the generation of aerosol species in coastal

423 suburban regions like ZH, which have sizable amounts of both sea salt and NO_x

424 emissions (Chatterjee et al., 2010; Liu et al., 2008).

425   Relative humidity exceeded 80% during the whole sampling time in ZH except

426 for 24th May, which was 64% and the air massed mainly came from northern

427 continental areas. The only other day that had a significant continental wind source at

428 ZH with a higher relative humidity (80%) was found on 7th June. The percentage of

429 chloride depletion was 95% and 69% for fine and coarse particles on 24th May and the

430 value was 78% and 64% on 7th Jun. There was no distinct difference found in coarse

431 particles for the two cases, there was a considerable difference in fine particles with

432 higher chloride depletion happened on 24th May. The meteorological conditions were

433 similar on these two days excluding humidity, moreover, the aerosol water content in

434 fine mode particles was about 8 times higher on 7th Jun. (3.6 μg m^{-3}) than that on 24th

435 May (0.45 μg m^{-3}). This finding suggested that humidity or aerosol water content

436 would be an important factor that affected the chloride depletion, which is consistent

437 with our understanding of the release of hydrochloric acid under the known high nitric

438 acid conditions, especially when there is less aerosol water (at relatively lower

439 humidity) to dissolve all of the volatiles, which would shift HNO_3 from gas- to

440 particle-phase and further to reinforce the release of hydrochloric acid (Chen et al.,

441   2013b; Dasgupta et al., 2007). In addition, the concentration of coarse mode nitrate

442   was similar for these two days with a value of 1.3~1.4 $\mu g\ m^{-3}$, but the concentration of

443   fine mode nitrate was bout 4 times higher on 24th May (0.18 $\mu g\ m^{-3}$) than that on 7th

444   Jun. (0.04 $\mu g\ m^{-3}$), further suggesting the relative lower humidity favor the particle

445   phase nitrate over chloride.

446

447   **3.5. The effects of long-range transport, and in-situ chemistry**

448   There were four days that the amounts and properties of the aerosols were

449   significantly impacted by long range transport and unique formation and alteration

450   mechanisms: one in each GZ and ZH (both occurring on 12th June) and three in JFM

451   (1st, 3rd, and 5th June).

452   On 12th June in both GZ and ZH, the total aerosol concentration was the highest

453   measured, at respectively 93.7 and 35.1 $\mu g\ m^3$ in GZ and ZH (Figure 2). Secondly,

454   the concentration of secondary soluble ions was the highest measured. The Sulfur

455   Oxidation Ratio (SOR) and Nitrogen Oxidation Ratio (NOR) are applied   to indicate

456   the degree of oxidation of SO_2 and NO_2 precursor gases (Wang *et al.,* 2005). The

457   equations for SOR and NOR are calculated as SOR=n-SO_4^{2-}/(n-SO_4^{2-}+n-SO_2) and

458   NOR=n-NO_3^-/(n-NO_3^-+n-NO_2, where n-SO_4^{2-} and n-NO_3^- are the molar concentrations

459   of particulate SO_4^{2-} and NO_3^- and n-SO_2 and n-NO_2 are the molar concentrations of

460   the precursor gases SO_2 and NO_2. SOR and NOR was also the highest On 12th June at

461   the range of 0.44-1.0 μm in GZ with the value of 0.20 and 0.17, respectively (Figure 6

462   (a-b)) (no supported data to estimate SOR and NOR in ZH on this day). Thirdly, this

463   was the only day in GZ that the nitrate size distribution was found to be uni-modal,

464   where it peaked in the 1.0-1.44µm size range (Figure 6 (d)), which was the largest of

465   any mean size nitrate in GZ measured. Meanwhile, the nitrate size distribution

466   changed from coarse mode to bi-modal and peaked in 0.25-0.44 µm size range in ZH

467   measured on this day (Figure S1(j)). Fourthly, the peak of sulfate and ammonia

468   shifted from typical values in the 0.44-1.0 µm size range to the 1.0-1.44 µm size range

469   (Take GZ for example, Figure 6(c) and Figure S1(f)). All of these are consistent with

470   enhanced secondary production. Such a statistically enhanced amount of secondary

471   production requires the aerosols to have had considerably more time in the

472   atmosphere to have aged as they have, and therefore is consistent with them having

473   undergone considerable long range transport (Cohen et al., 2011).

474   To provide further evidence, 3-day air mass backward trajectories were conducted

475   at each of the three sites. The parcels were released at initial heights of 100, 500,

476   1000 and 2000m, hourly, as a means of robustly sampling the boundary layer

477   throughout the day. The results showed that air masses winded up over GZ and ZH

478   in the lower free troposphere or near the top of the boundary layer had mostly

479   originated over continental Southeast Asia, while those winding up near the surface,

480   had mostly come from Northern China (Take GZ for example, Figure S1(a)).

481   Furthermore, since the air masses came from opposite directions at nearly the same

482   time, the end result was observed to be a stable meteorological condition over GZ

483   (very low wind 0.1 m s^{-1}) and ZH (wind speed was 1m/s which was the lowest

484   during the sampling times). In fact, it seems from the back trajectory analysis that

485   there was descending air in and around GZ and ZH on this day, which implies that

486   air transported from far away in the lower free-troposphere would have been

487   transported back near the surface (Take GZ for example, Figure S1 (b-c)).

488   FLEXPART-WRF was next applied to address the issue of the air residence time

489   through the column over GZ and ZH for that day. Take GZ for example, as can be

490   shown in Figure 6 (e-f), there was a strong influence from the local region of GZ and

491   surrounding adjoining cities, at a lower altitude (500m and lower) (Figure 6(e) and

492   Figure S1 (d-e)). All of these results were further consistent with the high levels of

493   aerosols measured as well as additional secondary processing having had time to

494   occur.

495   Except for in-situ formation, long-range transport was another impact factor. First,

496   HYSPLIT (Take GZ for example, Figure S1(a)) and FLEXPART-WRF (Figure 6(f))

497   showed that the air flow was mostly from Southeast Asia at levels over the boundary

498   layer ((Figure 6(f)), and hence had undergone long-range transport. Second, the

499   windspeed near the surface suddenly became very low. Therefore, there had been a

500   rapid change in the windspeed. Based on conservation laws for air mass, it would be

501   excepted for there to be some reasonable amount of mixing of the air vertically. This

502   was consistent with the finding that some of the air which has undergone long-range

503   transport would have mixed into the surface region. Furthermore, the ratio of OC to

504   EC concentrations was the minimum measured values on 12th June, with a mean

505   ratio of 1.32 and 2.39 in GZ and ZH, respectively. Also, OC showed a bi-modal

506   distribution, although predominantly in the fine mode while EC mostly peaked at

23

507　　fine mode particles (Take GZ for example, Figure S1 (g-h)), indicating that the

508　　organic aerosol was mostly primary, as would be expected from large fire sources.

509　　Additionally, the K^+ concentration on 12th June was about 2-3 times higher than that

510　　of mean value measured in GZ and ZH (Take GZ for example, Figure 10(a-b), and

511　　Figure S1(i)). Na^+ and Cl^- size distribution were found to be uni-modal distribution

512　　in GZ, where they peaked in the 1.0-1.44μm size range. Na^+ and Cl^- were bi-modal

513　　distribution in ZH on 12th Jun. (figures not showed here). All of these findings above,

514　　including the time of the year and the location, are consistent with the long-range

515　　transported biomass burning from Southeast Asia (Cohen, 2014).

516　　　At JFM the total aerosol concentration was highest on the 1st, 3rd, and 5th June. In

517　　particular, the levels of EC and potassium were elevated on all three days, and the

518　　ratio of OC to EC was depressed (Figure S2 (c-e)). However, in addition to these

519　　clues, there were some differences: the levels of sulfate and ammonia were

520　　remarkably elevated on the 3rd and 5th June (Figure 7(g) and Figure S2 (b)), likely due

521　　to a mixing of urban sources with the fire sources. On the other hand, on the 1st June,

522　　the sulfate was lower, but the nitrate was considerably higher, peaking in the coarse

523　　mode (Figure 7 (h)), likely due to mixing of South China Sea air with the fire sources.

524　　　HYSPLIT results showed that on all three of these days, the great majority of air

525　　masses arriving at JFM originated from continental Southeast Asia (Figure S2(a).

526　　However, all of these parcels of air arrived in the upper boundary layer or the lower

527　　free troposphere. By analyzing the FLEXPART-WRF runs at higher resolution, it was

528　　demonstrated that there was a strong influence of air from ocean on 1st June (Figure 7

529   (a-b)) at the lower parts of the boundary layer. This is consistent with the observed

530   non–elevated sulfate and elevated coarse nitrate on that day. Furthermore, the

531   FLEXPART-WRF runs at higher resolution demonstrated a considerable influence of

532   air from Southern China (urban and semi-urban Guangdong Province, including many

533   major shipping lanes) on the 3rd and 5th June, again in the lower parts of the boundary

534   layer (Figure 7(c-f)). This is again consistent with the observed elevated levels of

535   sulfate, due to the in-situ processing of urban emissions as the air was transported to

536   JFM, and then mixing with the fire emissions transported from the other direction at

537   height. Additionally, there was some amount of fine mode nitrate found on the 3rd Jun.,

538   further consistent with the in-situ processing of NO_2 emitted along with biomass

539   combustion, and therefore further evidence that mixing occurred between the two

540   different source regions.

541

542   **3.6. Quantifying the impacts of fires**

543   Taking a first look at the possibility that fires are responsible, as described above,

544   we look at a summary of the statistics of the MODIS Fire Hotspots (Figure 8). As we

545   observe, while the total number of fire hotspots occurring throughout Southeast Asia

546   is moderate in early May, the number reduces to the extent that there are effectively

547   almost no burning parcels. Furthermore, those few square kilometers that are burning

548   are of low radiative intensity, under 200W/m^2, and hence only moderately or lowly

549   emitting, with the exception of a single day in late June, after the period of interest

550   has ended. This result showed that the MODIS fire hotspots are not very useful in wet

551 and tropical regions. Since MODIS fire hotspots are obstructed by both clouds and

552 high levels of aerosols in the atmosphere, both of which are found associated with

553 tropical forest fires. Additionally, due to the highly wet ground surface, a significant

554 amount of the fires may low temperature and therefore not observable using the

555 MODIS sensors (Cohen, 2014, Giglio et al., 2006; Yu et al., 2015).

556 Instead, we follow the approach of Cohen (2014) and look at the once to twice

557 daily measured AOD data (Figure 9), in the context of the Empirical Orthogonal

558 Functions approach (EOF). Since MODIS fire hotspots are effectively point

559 measurements, and as such are not spatially robust, while AOD are continuous and

560 more easier to be observed, and provides more precise and robust spatial information

561 (Morisette et al., 2005a, 2005b; Levy et al., 2007, 2010; Remer et al., 2005).

562 Therefore, if a significant signal exists, it is far easier to track and transport, at the

563 scale of the inverse meteorological methods used here. The rationale is that over

564 Southeast Asia there are only a few known large urban centers (Hanoi, Ho Chi Minh

565 City, and Bangkok). Therefore, any other significant contribution to the variance of

566 measured AOD must be from fires. The EOF technique has been shown to be an

567 optimal manner by which to reproduce both the spatial extent and magnitude of the

568 smoke over Continental Southeast Asia (Cohen, 2014; Cohen and Leocure, 2015).

569 As observed, the major regions of high AOD (average AOD > 0.4) are found over

570 Southeast Asia as described above, with most of the sources coming from fires found

571 in two arcs: one from Eastern Thailand, through Laos, and ending in Central Vietnam;

572 and the other in the forests of Myanmar. The region around Hanoi is hard to decipher,

26

573 as it could be an urban expansion or fire. Additionally, there are regions found in

574 urban East Asia, including the region between Hong Kong and Guangzhou and

575 urbanization along the Yangtze River, however, all of these are known regions of

576 urbanization and are not regions where fire is important.

577   An EOF Analysis concludes that in fact these are the only two statistically

578 significant EOFs (Figure 10). The measured AOD over both of these regions is clearly

579 elevated compared with the region as a whole throughout the entire time. Furthermore,

580 there is an especially large contribution from these two EOFs compared with the

581 background over Southeast Asia only (excluding AOD measured over China, which is

582 downwind and hence not a fire source region) from May 31st to June 6th. Given the

583 rapid transport time from Southeast Asia to JFM, the fact that these peaks occur

584 within 1 day of the peaks in the fires is reasonable. Additionally, while the overall

585 Southeast Asian AOD drops from the 8th onwards, there is a very significant

586 difference (difference in AOD more than 0.5) between the overall AOD and that over

587 the two source regions again from June 8th to June 13th. Given that there are markers

588 of fires in GZ and ZH on June 12th, including high potassium and a low OC/EC ratio,

589 and that a significant portion of the airflow over these regions originated from

590 Southeast Asia within the past 72 hours, these results are consistent with high fires

591 originating from Southeast Asia, then being transported over the next 72 hours to GZ

592 and ZH. The fact that only one day has such measured conditions at the surface is

593 likely due to the fact that the smoke is mostly concentrated near the boundary layer

594 and hence local vertical mixing was most prevalent on or around June 12th.

27

595

4. Conclusion

Aerosol samples were collected at three sites using a 6-stage sampler during the local wet season in Southern China (May – Jun.) in 2010, to jointly study the mass and size distributions of aerosol chemical components. These site observations, together with model simulations and remote-sensing data, were used to investigate impacts of chemistry and atmospheric transport on the aerosol formation mechanisms at the three sites over Southern China. These were chosen such that they spanned different source and meteorological regions, at urban site GZ, a suburban site ZH, and a remote and forested site at JFM.

Sulfate and Ammonium were found to have a single peaked distribution from 0.44-1.0μm at all sites over the entire sampling period in this study, and accounted for 57.5-99 % of the daily-average total aerosol mass. Aqueous-phase reactions were found to be an essential factor to the formation of droplet sulfate. In addition, we found significant secondary processing and enhancement due to meteorological drivers which were wetter or allowed for a longer residence time.

A bi-modal distribution was found for nitrate, with a droplet mode in 0.44-1.0μm, indicating that it was formed under heavily polluted conditions or through similar secondary aerosol processing. On the other hand, nitrate had a significant fraction in the coarse mode in ZH and JFM during the wet season, where it accounted for about 40% of total mass. In this case, we found that the mass size distribution of nitrate was likely attributed to chloride depletion, with almost complete chloride depletion found

617 in ZH and JFM during the wet season. Additionally, relative humidity was an

618 important consideration in chloride depletion under relatively lower relative humidity,

619 conditions, leading to the increase of coarse mode nitrate.

620 OC and EC showed a broad peak at 0.25-1.0μm in GZ and ZH, consistent with

621 significant local sources, from urbanization, transport, residential, and shipping

622 sources. Furthermore, under less heavily polluted conditions, OC was found to have a

623 bi-modal distribution in JFM, with important contributions from secondary particle

624 formation in the fine mode and potential biological aerosol in the coarse mode

625 particles.

626 Additionally, OC and EC were shown to have broad peaks, and a significantly

627 different ratio, raising the likelihood of a mixing of the local emissions with emissions

628 transported long-range from biomass burning in Southeast Asia. These conditions

629 were further supported by a large amount of potassium found jointly with the aerosol.

630 An in-depth analysis of the meteorology, and remotely sensed Fire and AOD

631 properties, in conjunction with a variance maximizing technique, provided further

632 evidence to help us validate this assumption. It is clear that there was a significant

633 impact on GZ and ZH from fire sources from Thailand, Laos, and Vietnam, as well as

634 possible long-range transport of urban emissions from the urban megacity of Hanoi in

635 Vietnam. The combination of local formation and long-range transport played a

636 significant role on the variation of particle chemical compositions.

637 Overall, we found that the size distribution and formation of aerosols greatly

638 depend on emissions, location, and in-situ processing, especially aqueous-phase

639 reactions. Strong local formation and long-range-transport of both urban pollution

640 from GZ and of biomass burning from Southeast Asia all were observed to influence

641 the size distribution of chemical components across all of the area studies. On the

642 other hand, the interaction between sea salt aerosols and anthropogenic pollutants

643 showed significant effects at coastal locations and play an important role in the

644 deterioration of the air quality in Southern China under high relative humidity

645 conditions during the wet season.

646

655

656 **References**

657 Anlauf, K., Li, S.M., Leaitch, R., Brook, J., Hayden, K., Toom-Sauntry D., and Wiebe,

658 A.: Ionic composition and size characteristics of particles in the Lower Fraser

659 Valley: Pacific 2001 field study, Atmospheric Environment, 40, 2662- 2675, doi:

660 10.1016 /j.atmosenv. 2005.12.027, 2006.

661 Barth, M.C., Hegg, D.A., and Hobbs, P.V.: Numerical modeling of cloud and

662 precipitation chemistry associated with two rainbands and some comparisons with

663 observations, Journal of Geophysical Research, 97, 5825- 5845, doi:

664 10.1029/92JD00464, 1992.

665 Brioude, J., Arnold, D., Stohl, A., Gassiani, M., Morton, D., Seibert, P., Angevine, W.,

666 Evan, S., Dingwell, A., Fast, J.D., Easter, R.C., Pisso, I., Burkhart, J., and

667 Wotawo, G.: The Lagrangian particle disperation model FLEXPART-WRF

668 version 3.1, Geoscientific Model Development, 6, 1889-1904, doi: 10.5194/

669 gmd-6-1889-2013, 2013.

670 Burnett, R.T., et al.: An integrated risk function for estimating the global burden of

671 disease attributable to ambient fine particulate matter exposure, Environmental

672 Health Perspectives, 122, 397, doi:10.1289/ehp.1307049, 2014.

673 Cao, J.J., Lee, S.C., Ho, K.F., Zou, S.C., Fung, K., Li, Y., Watson, J.G., and Chow, J.

674 C.: Spatial and seasonal variations of atmospheric organic carbon and elemental

675 carbon in Pearl River Delta Region, China, Atmospheric Environment, 38, 4447–

676 4456, doi:10.1016/j.atmosenv.2004.05.016, 2004.

677 Chatterjee, A., Adak, A., Singh, A.K., Srivastava, M.K., Ghosh, S.K., Tiwari, S.,

678 Devara, P.C.S., and Raha, S.: Aerosol chemistry over a high altitude station at

679 northeastern Himalayas, India, PLoS ONE, 5, e11122, doi: 10.1371/journal.

680 pone.0011122, 2010.

681 Chen, S.Y., Huang, J.P., Zhao, C., Qian, Y., Leung, L.R. and Yang, B.: Modeling the

682 transport and radiative forcing of Taklimakan dust over the Tibetan Plateau: A

683   case study in the summer of 2006, Journal of Geophysical Research, 118, 797–

684   812, doi:10.1002/jgrd.50122, 2013a.

685   Chen, H.Z., Wu, D., Liao, B.T., Mao, X., Zhuang, H.B., Li, L., Liu, A.M., Li, H.Y.,

686   and Li, F.: Influence of different acidic gases and relative humidity on the chlorine

687   loss of marine aerosols, Acta Scientiae Circustantiae, 33, 1141-1149, 2013b (in

688   Chinese with English Abstract).

689   Clegg, S.L., Brimblecombe, P., and Wexler, A.S.: Thermodynamic Model of the

690   System $H^+−NH_4^+−SO_4^{2-}−NO_3^-−H_2O$ at Tropospheric Temperatures, The Journal

691   of Physical Chemistry A, 102, 2137-2154, doi: 10.1021/jp973042r, 1998.

692   Cohen J.B., and Lecoeur, E.: Decadal-scale relationship between measurements of

693   aerosols, land-use change, and fire over Southeast Asia, Atmospheric Chemistry

694   and Physics Discussion, 15, 26895-26957, doi:10.5194/acpd-15-26895-2015,

695   2015.

696   Cohen, J. B.: Quantifying the Occurrence and Magnitude of the Southeast Asian Fire

697   Climatology, Environmental Research Letter, 9, 114018, doi:10.1088/1748-9326/

698   9/11/114018, 2014.

699   Cohen, J. B., and Wang, C.: An Estimate of Global Black Carbon Emissions Using a

700   Top-Down Kalman Filter Approach, Journal of Geophysical Research , 119, 1-17,

701   doi:10.1002/2013JD019912, 2013.

702   Cohen, J. B., and Prinn, R.G.: Development of a fast, urban chemistry metamodel for

703   inclusion in global models, Atmospheric Chemistry and Physics, 11, 7629-7656,

704   doi:10.5194/acp-11-7629-2011, 2011.

705 Cohen, J. B., Prinn, R.G., and Wang, C.: The Impact of detailed urban-scale

706 processing on the composition, distribution, and radiative forcing of

707 anthropogenic aerosols, Geophysical Research Letters, 38, L10808,

708 doi:10.1029/2011GL047417, 2011.

709 Chung S.H., and Seinfeld, J.H.: Climate response of direct radiative forcing of

710 anthropogenic black carbon, Journal of Geophysical Research, 110, D11102, doi:

711 10.1029/2004JD005441, 2005.

712 Dasgupta, P.K., Campbell, S.W., Al-Horr, R.S., Ullah, S.M.R., Li, J.Z., Amalfitano, C.,

713 and Poor, N.D.: Conversion of sea salt aerosol to $NaNO_3$ and the production of

714 HCl: Analysis of temporal behavior of aerosol chloride/nitrate and gaseous

715 HCl/HNO_3concentrations with AIM, Atmospheric Environment, 41, 4242-4257,

716 doi:10.1016/j.atmosenv.2006.09.054, 2007.

717 Delene, D.J. and Ogren, J.A.:   Variability of aerosol optical properties at four North

718 American surface monitoring sites, Journal of the Atmospheric Sciences, 59,

719 1135-1150, doi: http://dx.doi.org/10.1175/ 1520-0469(2002)059 <1135:VOAOPA>

720 2.0.CO;2, 2002.

721 Draxler, R.R., and Hess, G.D.: An overview of the HYSPLIT_4 modeling system of

722 trajectories, dispersion, and deposition, Australian Meteorological Magazine, 47,

723 295-308, 1998.

724 Dubovik, O., Smirnov, A., Holben, B.N., King, M.D., Kaufman, Y.J., Eck, T.F., and

725 Slutsker, I.: Accuracy assessments of aerosol optical properties retrieved from

726 Aerosol Robotic Network (AERONET) Sun and sky radiance measurements,

727   Journal of Geophysical Research, 105, 9791-9806, doi: 10.1029/2000JD900040,

728   2000.

729   Ervens, B., Turpin, B.J., and Weber, R.J.: Secondary organic aerosol formation in

730   cloud droplets and aqueous particles (aqSOA): a review of laboratory, field and

731   model studies, Atmospheric Chemistry and Physics, 11, 11069-11102,

732   doi:10.5194/acp-11-11069-2011, 2011.

733   Giglio, L., Csiszar, I., and Justice, C.O.: Global distribution and seasonality of active

734   fires as observed with the Terra and Aqua Moderate Resolution Imaging

735   Spectroradiometer (MODIS) sensors, Journal of Geophysical Research, 111,

736   G02016, doi: 10.1029 / 2005JG000142, 2006.

737   Giglio, L., Kendall, J.D., and Mack, R.: A multi-year active fire data set for the tropics

738   derived from the TRMM VIRS, International Journal of Remote Sensing, 24,

739   4505- 4525, doi: 10.1080/0143116031000070283, 2003.

740   Han, Y., Han, Z., Cao, J.J., Chow, J.C., Watson, J.G., An, Z.S., Liu, S.X., and Zhang,

741   R.J.: Distribution and origin of carbonaceous aerosol over a rural high-mountain

742   lake area, Northern China and its transport significance, Atmospheric

743   Environment, 42, 2405-2414, doi:10.1016/j.atmosenv.2007.12.020, 2008.

744   Harrison, R.M., and Pio, C.A.: Size differentiated composition of inorganic

745   atmospheric aerosols of both marine and polluted continental origin, Atmospheric

746   Environment, 17, 1733-1738, doi:10.1016/0004-6981(83)90180-4, 1983.

747   Heald, C.L. and Spracklen, D.V.: Atmospheric budget of primary biological aerosol

748   particles from fungal spores, Geophysical Research Letters, 36, L09806, doi:

749   10.1029/2009GL037493, 2009.

750   Huang, J.P., Wang, T.H., Wang, W.C., Li, Z.Q. and Yan, H.R.: Climate effects of dust

751   aerosols over East Asian arid and semiarid regions, Journal of Geophysical

752   Research, 119, 11398–11416, doi: 10.1002/2014JD021796, 2014.

753   Huang, X.F., Yu, J.Z., He, L.Y., and Hu. M.,: Size distribution characteristics of

754   elemental carbon emitted from Chinese vehicles: results of a tunnel study and

755   atmospheric implications, Environmental Science & Technology, 44, 5355–5360,

756   doi: 10. 1021 /es0607281, 2006.

757   Huang, Z.E., Harrision, R.M., Allen, A.G., James, J.D., Tilling, R.M. and Yin, J.X.:

758   Field intercomparison of filter pack and impactor sampling for aerosol nitrate,

759   ammonium, and sulphate at coastal and inland sites, Atmospheric Research, 71,

760   215-232, doi:10.1016/j.atmosres.2004.05.002, 2004.

761   Hsu, S.C., Liu, S.C., Kao, S.J., Jeng, W.L., Huang, Y.T., Tseng, C.M., Tsai, F.J., Tu,

762   J.Y., and Yang, Y.: Water-soluble species in the marine aerosol from the northern

763   South China Sea: High chloride depletion related to air pollution, Journal of

764   Geophysical Research, 112, D19304, doi:10.1029/2007JD008844,2007.

765   Kim, S.W., Berthier, S., Raut, J.C., Chazette, P., Dulac, F., and Yoon, S.C.: Validation

766   of aerosol and cloud layer structures from the space-borne lidar CALIOP using a

767   ground-based lidar in Seoul, Korea, Atmospheric Chemistry and Physics, 8,

768   3705-3720, doi:10.5194/acp-8-3705-2008, 2008.

769   Jacobson, M.Z.:   Global direct radiative forcing due to multicomponent

770   anthropogenic and natural aerosols, Journal of Geophysical Research, 106,

771   1551-156, doi: 10.1029/2000JD900514, 2001.

772   Lan, Z.J., Chen, D.L., Li, X., Huang, X.F., He, L.Y., Deng, Y.G., Feng, N., and Hu, M.:

773   Modal characteristics of carbonaceous aerosol size distribution in an urban

774   atmosphere of South China, Atmospheric Research, 100, 51-60,

775   doi:10.1016/j.atmosres.2010.12.022, 2011.

776   Levy, R., Remer, L., Kleidman, R., et al.: Global evaluation of the Collection 5

777   MODIS darktarget aerosol products over land, Atmospheric Chemistry and

778   Physics, 10, 10399-10420, doi:10.5194/acp-10-10399-2010, 2010.

779   Levy, R., Remer, L., and Dubovik, O.: Global aerosol optical properties and

780   application to Moderate Resolution Imaging Spectroradiometer aerosol retrieval

781   over land, Journal of Geophysical Research, 112, 1-15, doi:

782   10.1029/2006JD007815, 2007.

783   Lim, Y.B., Tan, Y., Perri, M.J., Seitzinger, S.P., and Turpin, B.J.: Aqueous chemistry

784   and its role in secondary organic aerosol (SOA) formation, Atmospheric

785   Chemistry and Physics, 10, 10521-10539, doi: 10.5194/acp-10-10521-2010, 2010.

786   Liu, Y., Huang, J., Shi, G., Takamura, T., Khatri, P., Bi, J., Shi, J., Wang, T. Wang, X.,

787   and Zhang B.: Aerosol optical properties and radiative effect determined from

788   sky-radiometer over Loess Plateau of Northwest China, Atmospheric Chemistry

789   and Physics, 11, 11455–11463, doi: 10.5194/acp-11-11455-2011, 2011.

790   Liu, S., Hu, M., Slanina, S., He, L.Y., Niu, Y.W., Bruegemann, E., Gnauk, T. and

791   Herrmann, H.: Size distribution and source analysis of ionic compositions of

792   aerosols in polluted periods at Xinken in Pearl River Delta (PRD) of China,

793   Atmospheric Environment, 42, 6284-6295, doi: http://dx.doi.org/10.1016/j.

794   atmosenv.2007.12.035, 2008.

795   Lu, Q., Zheng, J.Y., Ye, S.Q., Shen, X.L., Yuan, Z.B. and Yin, S.S.: Emission trends

796   and source characteristics of SO_2, NOx, PM_{10} and VOCs in the Pearl River Delta

797   region from 2000 to 2009, Atmospheric Environment, 76, 11-20, doi:

798   http://dx.doi.org/10.1016/j.atmosenv.2012.10.062, 2013.

799   Meng, Z., and Seinfeld, J.H.: On the source of the submicrometer droplet mode of

800   urban and regional aerosols, Aerosol Science and Technology, 20, 253- 265, doi:

801   10.1080 /02786829408959681, 1994.

802   Myhre, G., et al.: Radiative forcing of the direct aerosol effect from AeroCom Phase

803   II simulations, Atmospheric Chemistry and Physics, 13, 1853-1877,

804   doi:10.5194/acp-13-1853-2013, 2013.

805   Morisette, J.T., Giglio, L., Csiszar, I. and Justice, C.O.: Validation of the MODIS

806   active fire product over Southern Africa with ASTER data, International Journal

807   of Remote Sensing, 26, 4239-4264, doi: 10.1080/01431160500113526, 2005a.

808   Morisette, J.T., Giglio, L., Csiszar, I., Setzer, A., Schroeder, W., Morton, D. and

809   Justice, C.O.: Validation of MODIS active fire dectection productes derived from

810   two algorithms, Earth Interaction, 9, 1-23, doi: http://dx.doi.org/10.1175/EI141.1,

811   2005b.

812   Petrenko, M., Kahn, R., Chin, M., Soja, A., Kucsera, T., and Harshvardhan,: The use

813   of satellite-measured aerosol optical depth to constrain biomass burning emissions

814   source strength in the global model GOCART, Journal of Geophysical Research,

815   117, D18212, doi: 10.1029/2012JD017870, 2012.

816   Pierson, W.R., and Brachaczek, W.W.: Coarse and fine particle atmospheric nitrate

817   and HNO$_3$(g) in Claremont, California, during the 1985 nitrogen species methods

818   comparison study, Atmospheric Environment, 22, 1665–1668, doi:10.1016/

819   0004-6981(88)90394-0, 1998.

820   Pillai, P.S., and Moorthy, K.K.: Aerosol mass-size distributions at a tropical suburban

821   environment: response to mesoscale and synoptic processes, Atmospheric

822   Environment, 35, 4099- 4112, doi:10.1016/S1352-2310(01)00211-4, 2001.

823   Pio, C., Legrand, M., Oliveira, T., Afonso, J., Santos, C., Caseiro, A., Fialho, P.,

824   Barata, F., Puxbaum, H., Sanchez-Ochoa, A., Kasper-Giebl, A., Gelencsér, A.,

825   Preunkert, S., and Schock, M.: Climatology of aerosol composition (organic

826   versus inorganic) at nonurban sites on a west–east transect across Europe, Journal

827   of Geophysical Research-Atmosheres, 112, D23S02, 10.1029/2006JD008038,

828   2007.

829   Ramanathan, V., and Garmichael, G.: Global and regional climate changes due to

830   black carbon, Nature Geoscience, 1, 221-227, doi:10.1038/ngeo156, 2008.

831   Remer, L.A., Mattoo, S., Levy, R.C., Munchak, L.A.: MODIS 3km aerosol product:

832   algorithm and global perspective, Atmospheric Measurement Techniques, 6,

833   1829–1844, doi:10.5194/amt-6-1829-2013, 2013.

834   Remer, L., Kaufman, Y., Tanre, D., Mattoo, S., Chu, D.A., Martins, J.V., Li, R.R.,

835   Ichoku, C., Levy, R.C., Kleidman, R.G., Eck, T.F, Vermote, E. and Holben, B.N.:

836   The MODIS Aerosol Algorithms, Products, and Validation, Jouranl of

Atmospheric Science, 62, 947-973, doi: 10.1175/JAS3385.1, 2005.

Rosenfeld, D., Sherwood, S., Wood, R., and Donner, L.: Climate effects of aerosol-cloud interactions, Science, 343, 379-380, doi: 10.1126/science.1247490, 2014.

Schuster, G.L., Dubovik, O., and Holben, B.N.: Angstrom exponent and bimodal aerosol size distributions, Journal of Geophysical Research, 111, D07207, doi: 10. 1029 /2005JD006328, 2006.

Seinfeld, J., and Pandis, S.: Atmospheric Chemistry and Physics: From Air Pollution to Climate Change, John Wiley & Sons, New York, 2006.

Situ, S.P, Guenther, A., Wang, X.M., Jiang, X.X., Turnipseed, A., Wu, Z.Y., Bai, J.H., and Wang, X.X.: Impacts of seasonal and regional variability in biogenic VOC emissions on surface ozone in the Pearl River delta region, China, Atmospheric Chemistry and Physics, 13, 11803- 11817, doi:10.5194/acp-13-11803-2013, 2013.

Stelson, A.W. and Seinfeld, J.H.: Relative humidity and temperature dependence of the ammonium nitrate dissociation constant, Atmospheric Environment, 16, 983-992, doi:10.1016/0004-6981(82)90184-6, 1982.

Stohl, A., Hittenberer, M., and Wotawa, G.: Validation of the Lagrangian particle dispersion model Flexpart against large-scale tracer experiment data, Atmospheric Environment, 32, 4245-4264, doi:10.1016/S1352-2310(98)00184-8, 1998.

Tao, J., Ho, K.F., Chen, L.G., Zhu, L.H., Han, J.L., and Xu, Z.C.: Effect of chemical composition of $PM_{2.5}$ on visibility in Guangzhou, China, 2007 Spring, Particulogy, 7, 68-75, doi: 10.1016/j.partic.2008.11.002, 2009.

Tsigaridis, K., et al.: The AeroCom evaluation and intercomparison of organic aerosol

859   in global models, Atmospheric Chemistry and Physics, 14, 10845-10895,

860   doi:10.5194/acp-14-10845-2014, 2014.

861 Volkamer, R., Ziemann, P.J., and Molina, M.J.: Secondary Organic Aerosol Formation

862   from Acetylene (C_2H_2): seedeffect on SOA yields due to organic photochemistry

863   in the aerosol aqueous phase, Atmospheric Chemistry and Physics, 9, 1907-1928,

864   doi: 10.5194/acp-9-1907-2009, 2009.

865 Wang, X.F., Wang, W.X., Yang, L.X., Gao, X.M., Nie, W., Yu, Y.C., Xu, P.J., Zhou, Y.,

866   and Wang, Z.: The secondary formation of inorganic aerosols in the droplet mode

867   through heterogeneous aqueous reactions under haze conditions, Atmospheric

868   Environment, 63, 68-76, doi: 10.1016/j.atmosenv.2012.09.029, 2012.

869 Wang, Z., et al.: Source and variation of carbonaceous aerosols at Mount Tai, North

870   China: results from a semi-continuous instrument, Atmospheric Environment, 45,

871   1655-1667, doi: 10.1016/j.atmosenv.2011.01.006, 2011.

872 Wang, Y., Zhuang, G.S., Tang, A.H., Yuan, H., Sun, Y.L., Chen, S. and Zheng, A.H.:

873   The ion chemistry and the source of $PM_{2.5}$ aerosol in Beijing, Atmospheric

874   Enviornment, 39, 3771-3784, doi:10.1016/j.atmosenv.2005.03.013, 2005.

875 Yang, X. and Wenig, M.: Study of columnar aerosol size distribution in Hong Kong,

876   Atmospheric Chemistry and Physics, 9, 6175-6189, doi:10.5194/acp-9-6175-2009,

877   2009.

878 Yao, X.H., Ling, T.Y., Fang, M. and Chan, C.K.: Comparison of thermodynamic

879   predictions for in situ pH in $PM_{2.5}$, Atmospheric Environment, 40, 2835-2844,

880   doi:10.1016/j.atmosenv.2006.01.006, 2006.

881   Yao, X.H., Lau, A.P.S., Fang, M., Chan, C.K., and Hu, M.: Size distributions and

882   formation of ionic species in atmospheric particulate pollutants in Beijing, China:

883   2—dicarboxylic acids, Atmospheric Environment, 37, 3001-3007, doi:10.1016/

884   S1352-2310(03)00256-5, 2003a.

885   Yao, X.H., Fang, M. and Chan, C.K. The size dependence of chloride depletion in fine

886   and coarse sea-salt particles, Atmospheric Environment, 37, 742-751,

887   doi:10.1016/S1352-2310(02)00955-X, 2003b.

888   Yu, C., Chen, L.F., Li, S.S., Tao, J.H. and Su, L.: Estimating Biomass Burned Areas

889   from Multispectral Dataset Detected by Multiple-Satellite, Spectroscopy and

890   Spectral Analysis, 35, 739-745, doi:10.3964/j.issn.1000-0593(2015)03-0739 -07,

891   2015.

892   Zhang, Z.S., Engling, G., Zhang, L.M., Kawamura, K., Yang, Y.H., Tao, J., Zhang,

893   R.J., Chan, C.Y. and Li, Y.D.: Significant influence of fungi on coarse

894   carbonaceous and potassium aerosols in a tropical rainforest, Environmental

895   Research Letters, 10, 034015, doi:10.1088/1748-9326/10/3/034015, 2015.

896   Zhang, Z.S., Engling, G., Chan, C.Y., Yang, Y.H., Lin, M., Shi, S., He, J., Li, Y.D.,

897   and Wang, X.M.: Determination of isoprene-derived secondary organic aerosol

898   tracers (2-methyltetrols) by HPAEC-PAD: Results from size-resolved aerosols in a

899   tropical rainforest, Atmospheric Environment, 70, 468- 476, doi:10.1016/

900   j.atmosenv. 2013.01.020, 2013a.

901   Zhang, Q., Tie, X.X., Lin, W.L., Cao, J.J., Quan, J.N., Ran, L., and Xu, W.Y.:

902   Variability of SO_2 in an intensive fog in North China Plain: Evidence of high

903   solubility SO$_2$, Particuology, 11, 41-47, doi:10.1016/j.partic.2012.09.005, 2013b.

904   Zhao, Y.L., and Gao, Y.: Mass size distributions of water-soluble inorganic and

905   organic ions in size-segregated aerosols over metropolitan Newark in the US east

906   coast,   Atmospheric   Environment,   42,   4063-4078,

907   doi:10.1016/j.atmosenv.2008.01.032, 2008a.

908   Zhao, Y.L., and Gao, Y.: Acidic species and chloride depletion in coarse aerosol

909   particles in the US east coast, Science of The Total Environment, 407, 541- 547,

910   doi:10.1016/j.scitotenv.2008.09.002, 2008b.

911   Zheng, J.Y., He, M., Shen, X.L., Yin, S.S., and Yuan, Z.B.: High resolution of black

912   carbon and organic carbon emissions in the Pearl River Delta region, China,

913   Science of The Total Environment, 438, 189-200, doi: http://dx.doi.org/10.1016/j.

914   scitotenv.2012.08.068, 2012.

915   Zheng, J.Y., Zhang, L.J., Che, W.W., Zheng, Z.Y. and Yin, S.S.: A highly resolved

916   temporal and spatial air pollutant emission inventory for the Pearl River Delta

917   region, China and its uncertainty assessment, Atmospheric Environment, 43,

918   5112- 5122, doi: http://dx.doi.org/10.1016/j.atmosenv.2009.04.060, 2009.

919   Zhou, S.Z., Davy, P.K., Wang, X.M., Cohen, J.B., Liang, J.Q., Huang, M.J., Fan, Q.,

920   Chen, W.H. Chang, M., Ancelet, T. and Trompetter, W.J.: High time-resolved

921   elemental components infine and coarse particles in the Pearl River Delta region

922   of Southern China: Dynamic variations and effects of meteorology, Science of the

923   Total Environment, doi: 10.1016/j.scitotenv.2016.05.194, 2016 (in press).

924   Zhou, Y., Xue, L.K., Wang, T., Gao, X.M., Wang, Z., Wang, X.F., Zhang, J.M., Zhang,

925   Q.Z., and Wang, W.X.: Characterization of aerosol acidity at a high mountain site

926   in central eastern China, Atmospheric Environment, 51, 11-20,

927   doi:10.1016/j.atmosenv.2012.01.061, 2012.

928 Zhuang, H., Chan, C.K., Fang, M., Wexler, A.S.: Size distributions of particulate

929   sulfate, nitrate and ammonium at a suburban site in Hong Kong, Atmospheric

930   Environment,33, 843- 853, doi:10.1016/S1352-2310(98)00305-7, 1999.

931 **Figures**

932 **Figure 1.** Location of sampling sites in Southern China: GZ (Guangzhou), ZH
933   (Zhuhai), and JFM (Jianfeng Mountain) and their surrounding environments
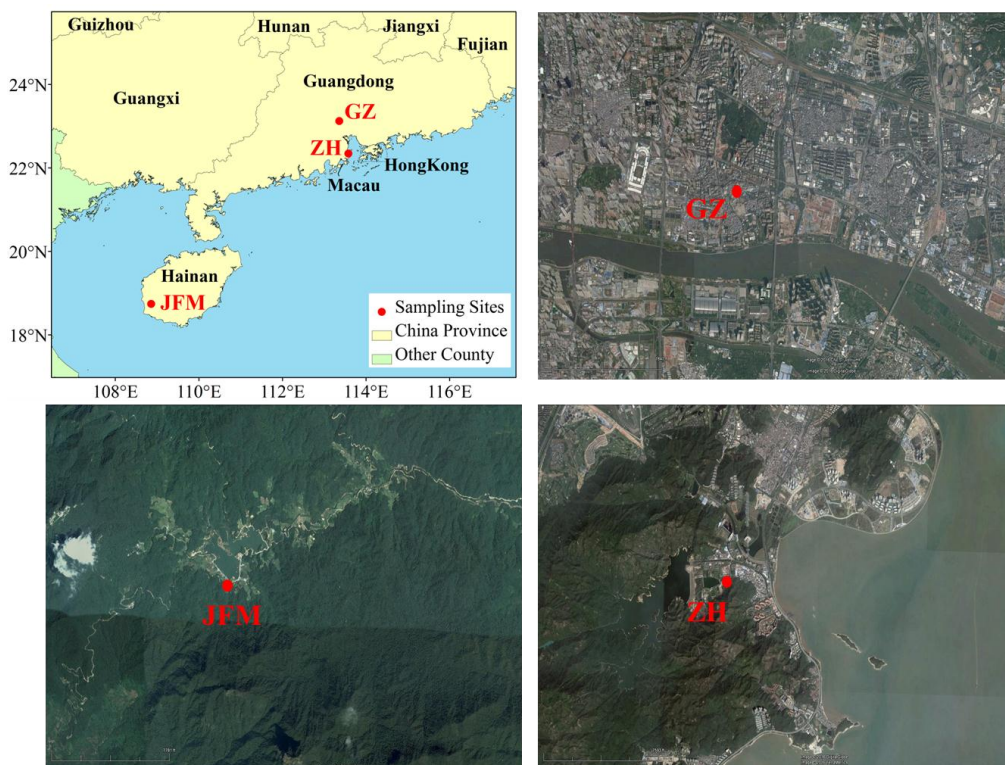
934
935
936
937
938
939
940
941
942
943
944
945
946
947
948
949
950
951
952
953
954
955

956 **Figure 2.** Time series of PM$_{18}$ chemical compositions at the three sites during the

957 2010 wet season.
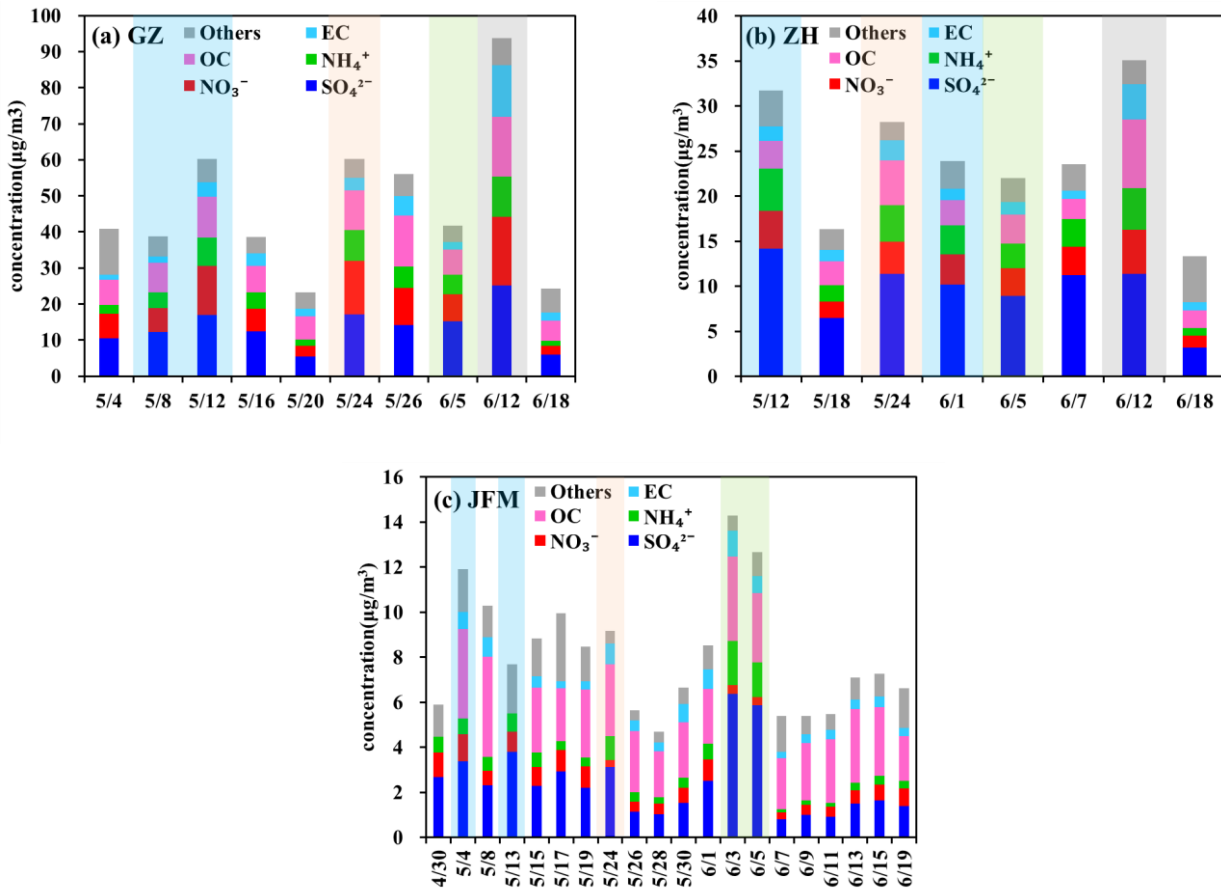
958
959
960
961
962
963
964
965
966
967
968
969
970
971
972
973
974
975

976   **Figure 3.** The mass size distribution of major compositions (SO_4^{2-}, NO_3^-, NH_4^+, OC
977   and EC) at the three sites during study period (SO_4^{2-} is plotted against the right
978   Y-Axes)
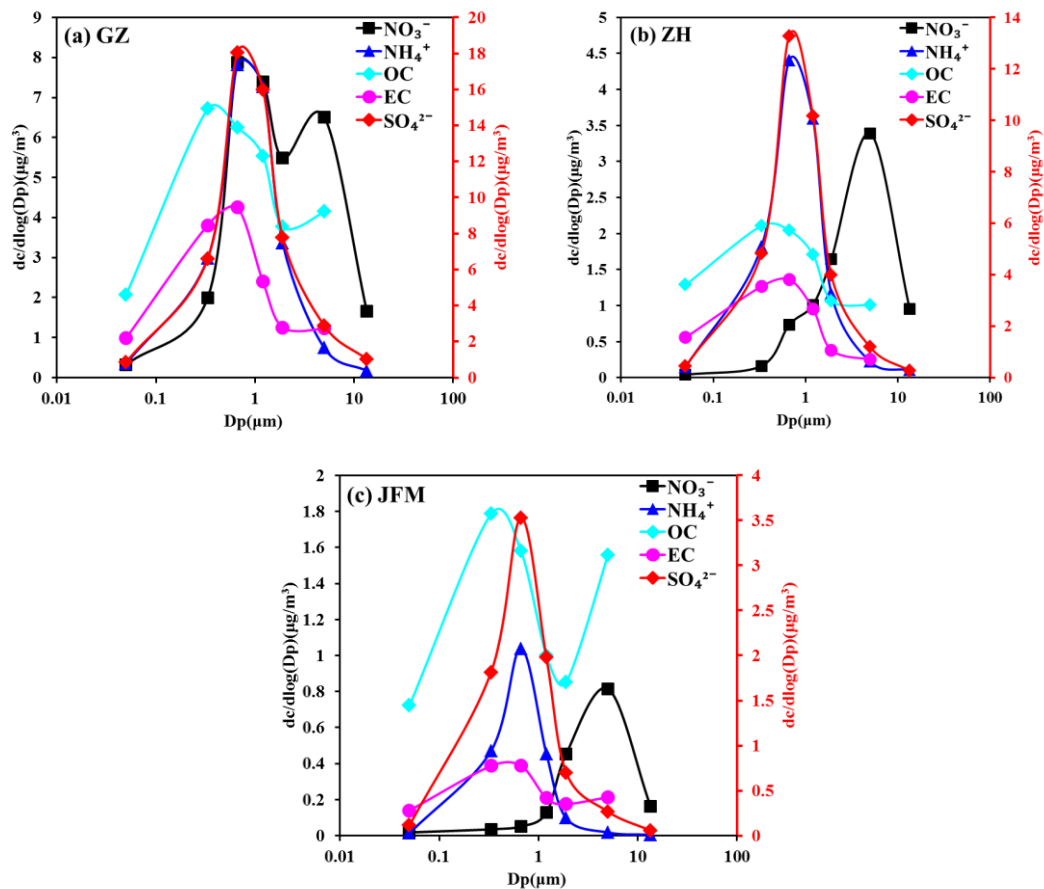
979

980 **Figure 4.** Case study on 8th May. in GZ ((a)The cloud fraction over Southern China;

981 (b)Distribution of simulated average 2 m relative humidity at 05:00-07:00 LT; (c) The

982 time series of observational visibility, wind speed, relative humidity and the

983 depression of dew point (time resolution was 30mins); (d) The time series of

984 monitoredmean SO_2 during 2009-2010 and SO_2 on 8th May ;(e) Distribution of

985 simulated average cloud; (f) The time-height distribution of simulated cloud water

986 mixing ratio on 8th May; (g-h) The time-height of simulated Aitken and accumulation

987 mode SO_4^{2-})

Cloud Water Mixing Ratio(g/kg)

Cloud Water Mixing Ratio(g/kg)

Aitken mode SO$_4^2$ (μg/m^3)

Accumulation mode SO$_4^2$ (μg/m^3)
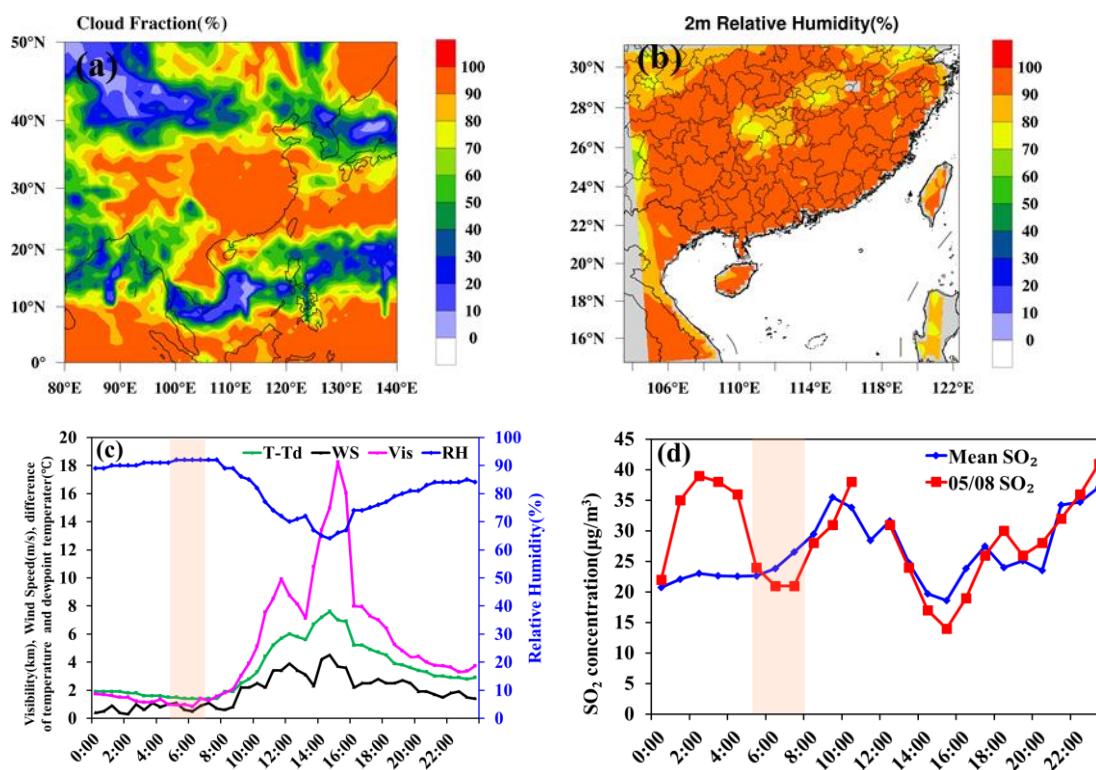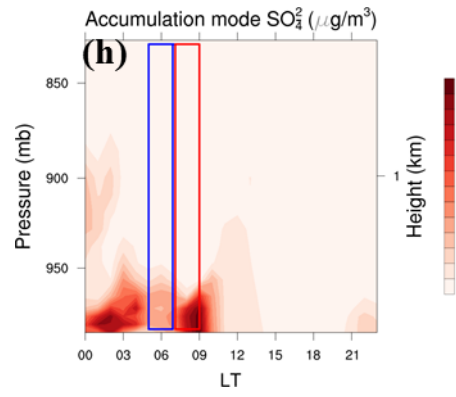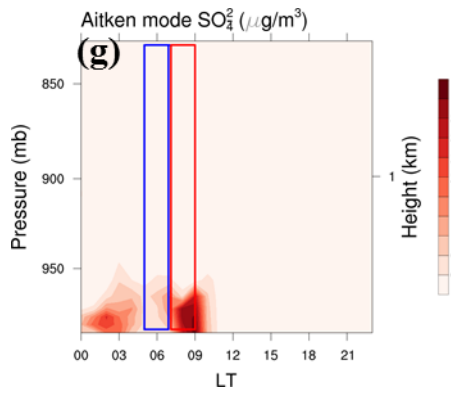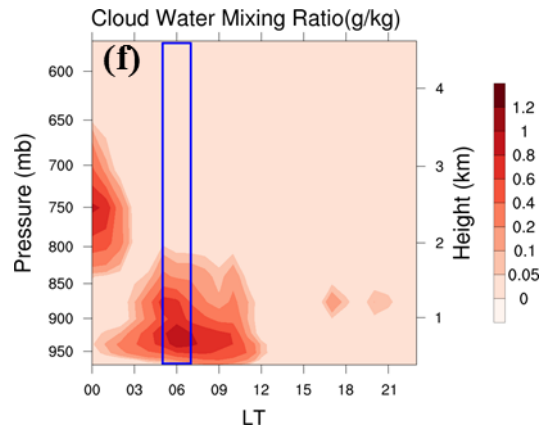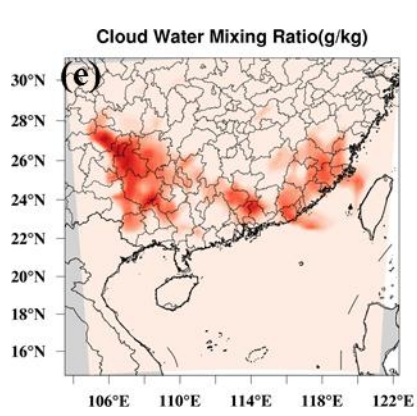
988

989   **Figure 5.** The mass size distribution of (a-c) Na$^+$ and Cl$^-$ and (d) percentage of
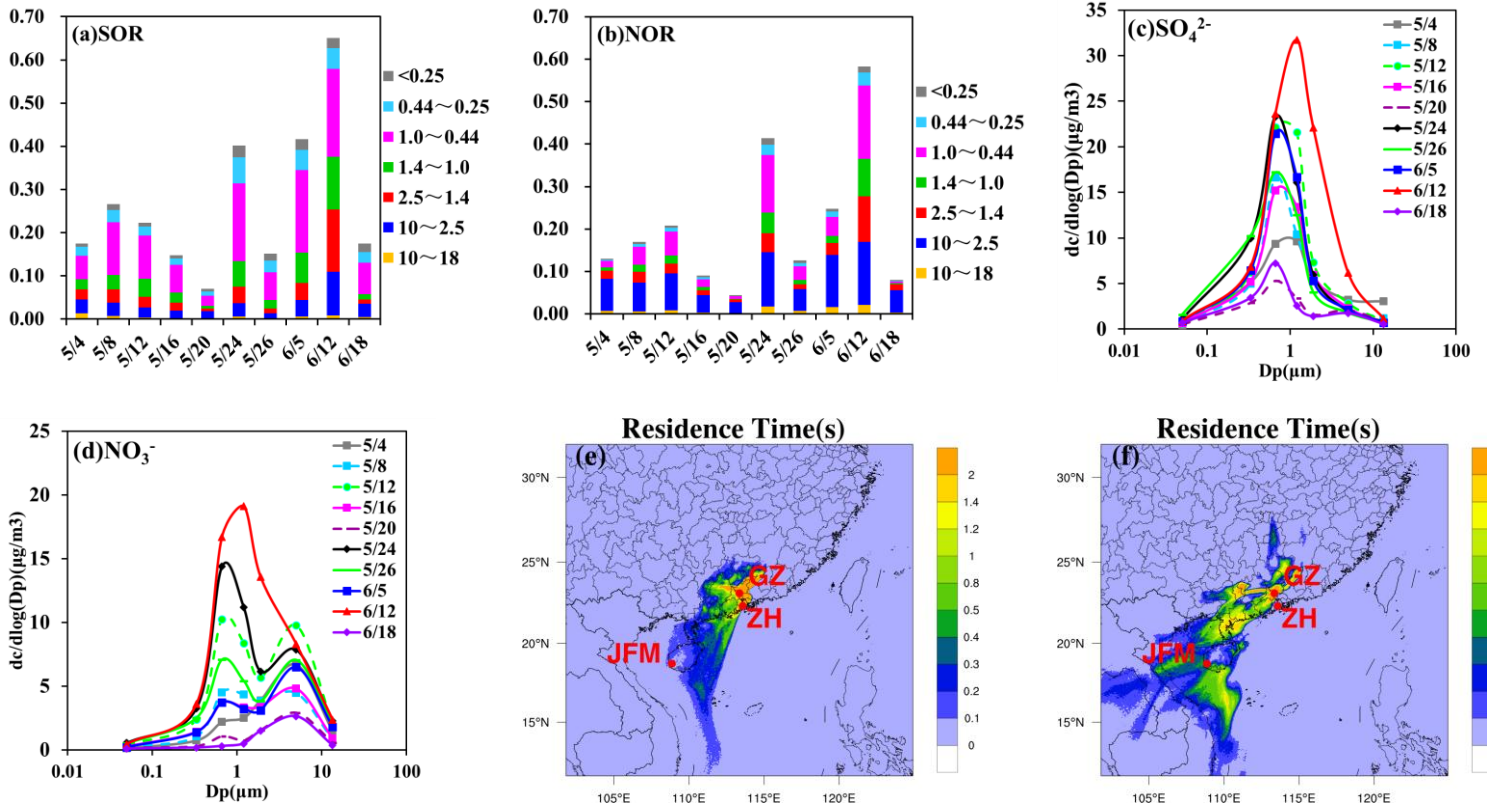990   chloride depletion at the three sites
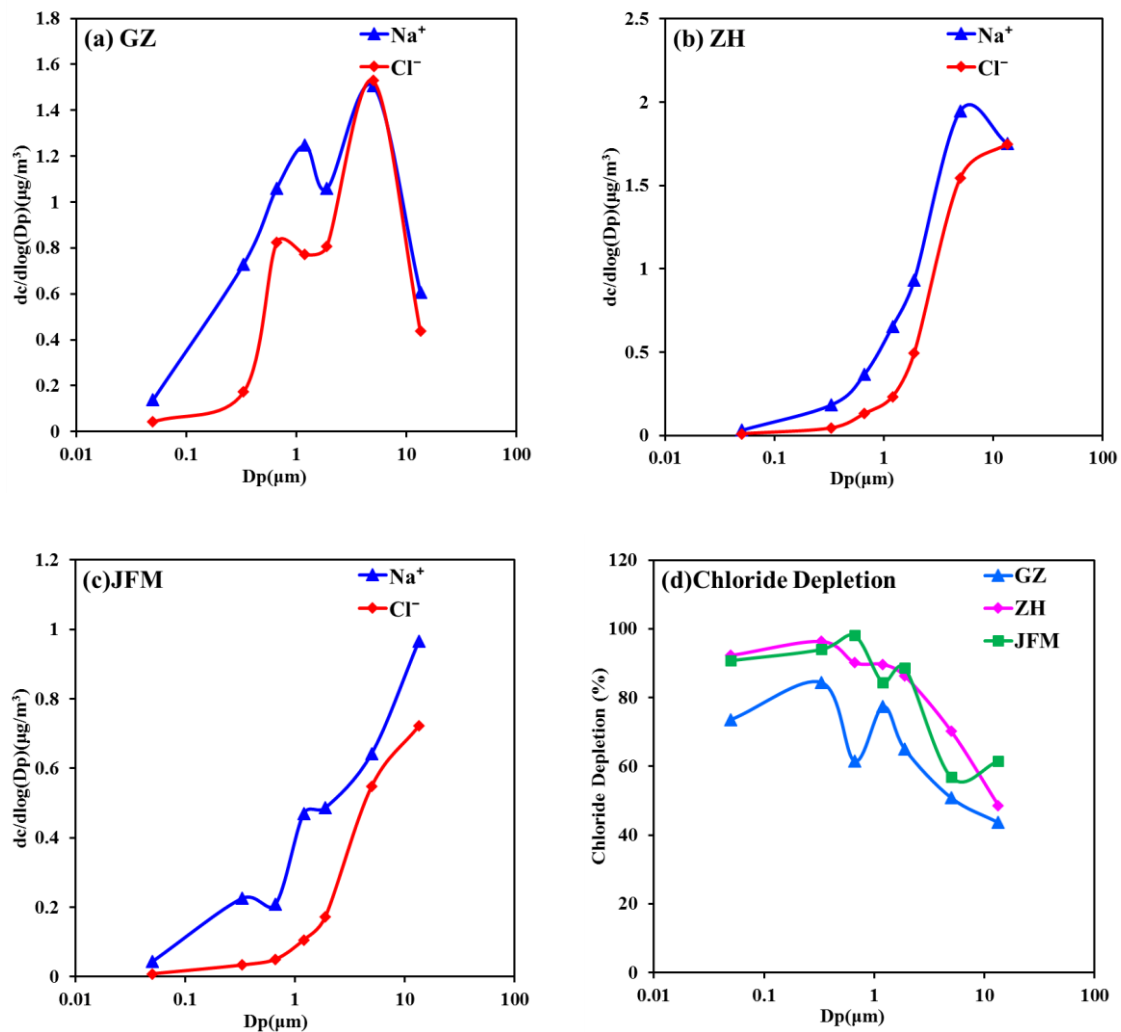
991

992

993

994　**Figure 6.** Case study on 12th Jun. in GZ ((a-b) The time series of SOR and NOR; (c-d)

995　The mass size distribution of SO_4^{2-} and NO_3^-; (e-f) FLEXPART-WRF total column

996　residence times over the last 72h arriving in GZ on 12th Jun. at 100m and 1000m)

997

Figure 7. Case study on 1st, 3rd and 5th Jun. in JFM ((a-b) FLEXPART-WRF total

999   column residence times on over the last 72h arriving in JFM on 1st Jun. at 100m and

1000   1000m; (c-d) and (e-f) same at (a-b) but on 3rd and 5^{th}Jun. respectively; (g-h) The

1001   mass size distribution of SO_4^{2-} and NO_3^-)
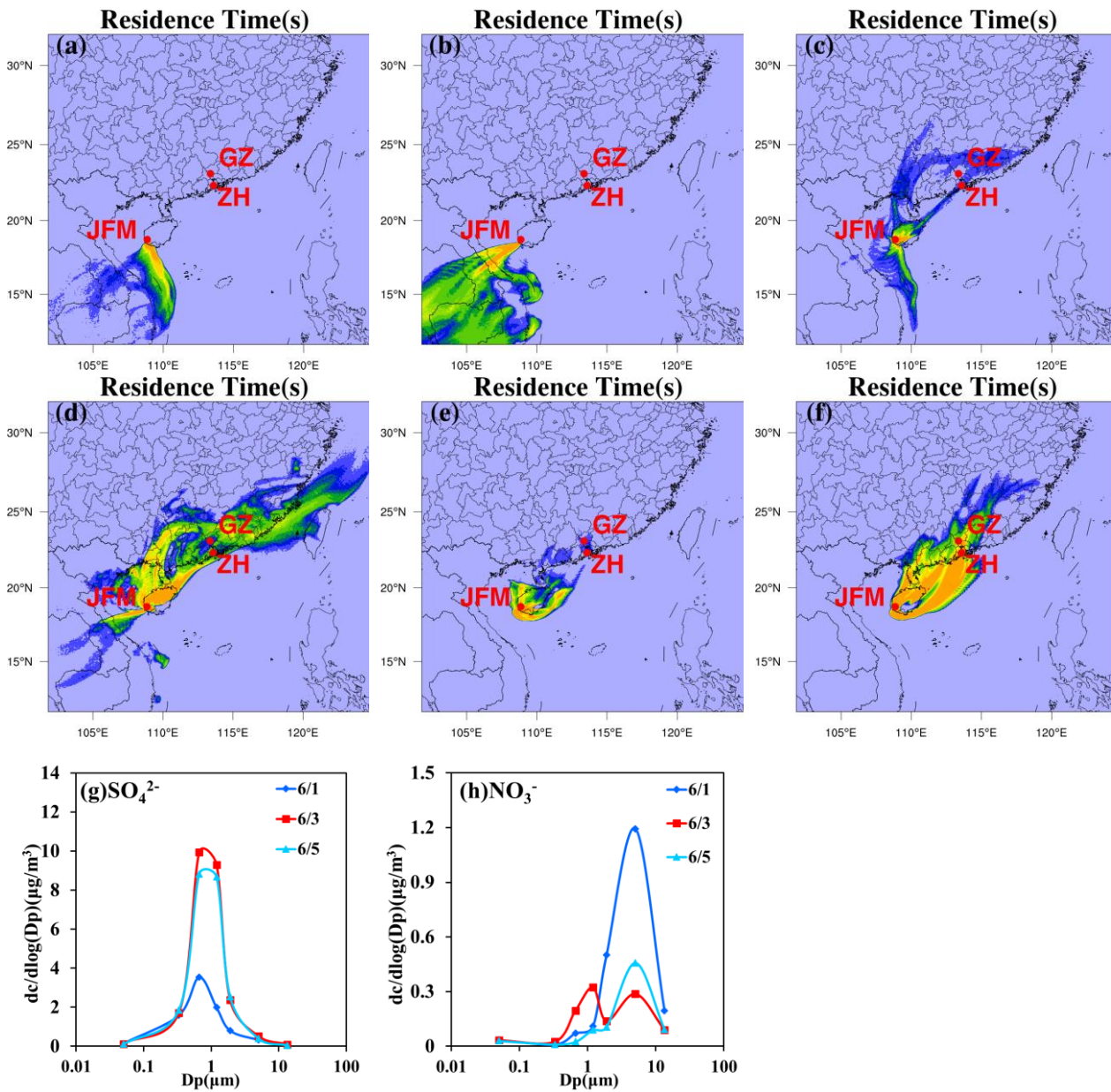
1002

1003

1004

1005   **Figure 8.** Spatially averaged/aggregated statistics of (a) MODIS Fire numbers (Count)

1006   and (b) Fire Radiative Power (FRP) over Southeast Asia for May and June 2010. The

1007   statistics represent the respective Count [total number of burning 1kmx1km pixels]

1008   and average FRP [W/m^2 per 1kmx1km pixel] over the whole of Southeast Asia and

1009   the specific regions where the AOD (as an indicator for smoke) has its highest levels

1010   of variability: EOF1 and EOF2.
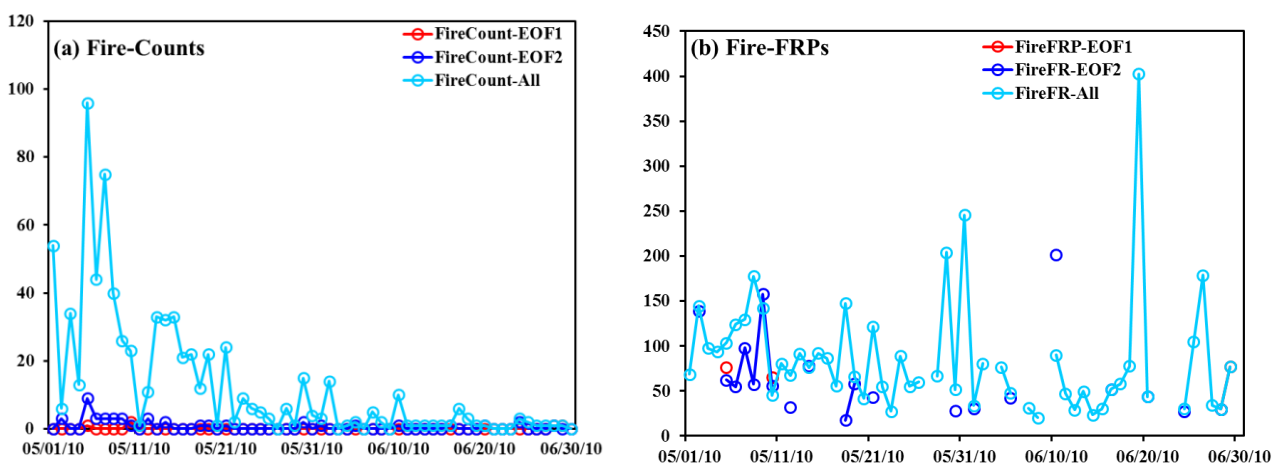
1011

1012

1013

1014

1015

1016

1017

1018

1019   **Figure 9.** Average spatial distribution of the (a) mean and (b) standard deviation of

1020   daily MODIS AOD from May 1st through June 30th 2010
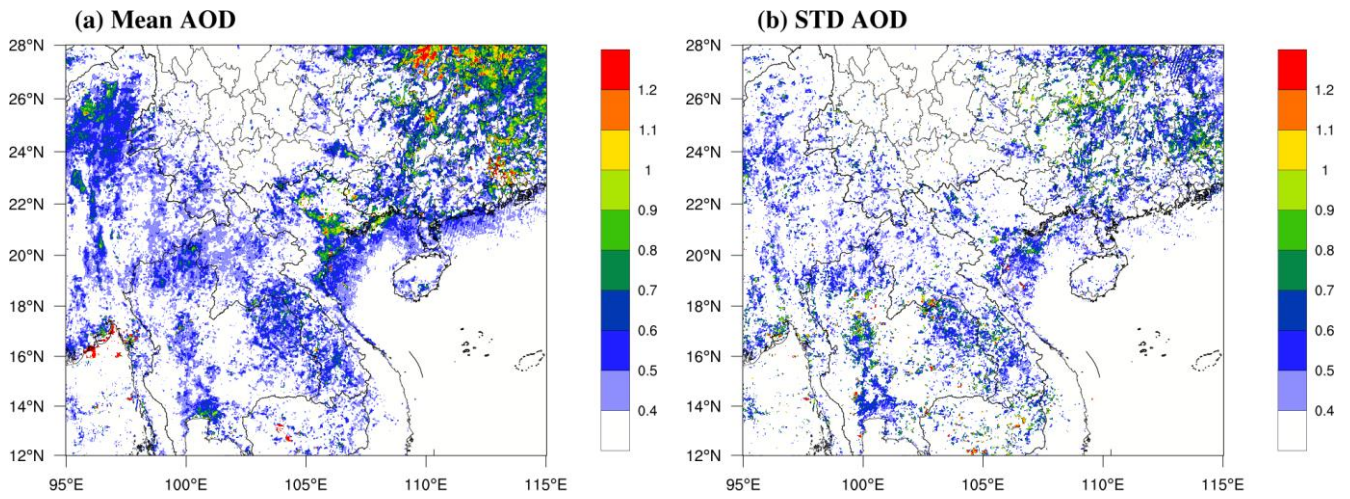
1021
1022
1023
1024
1025
1026
1027
1028
1029
1030
1031
1032
1033

1034 **Figure 10**. The time-varying statistics of the AOD averaged over the first two EOFs

1035 of the AOD (reflecting the regions most impacted by AOD variance or smoke from

1036 fires) and the average K$^+$ concentration and average ratio of OC/EC in the three sites.
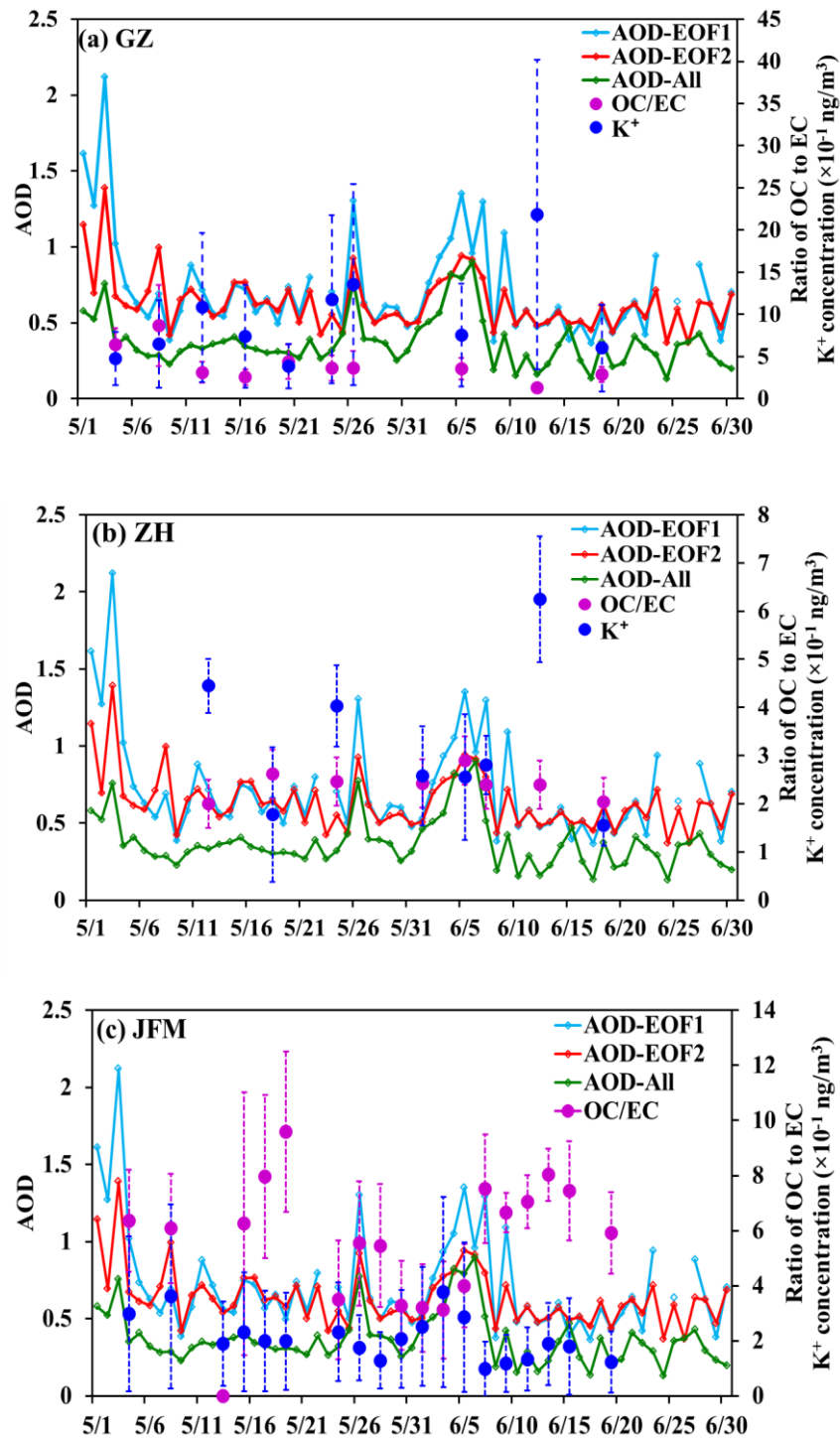
1037

1038 **Tables**

1039 **Table 1.** Average concentration and standard deviation $[\mu g\ m^{-3}]$ of chemical

1040 components in the given size-resolved particles (and their percentage of PM_{10}) at the

1041 three sites during the 2010 wet season.

Site	Size	Sum of measured species	SO_4^{2-}	NO_3^-	NH_4^+	OC	EC
GZ	$PM_{1.0}$	24.4±10.9	8.0±3.1 (60.2)	3.0±2.4 (34.5)	3.4±1.7 (64.2)	5.5±2.0 (57.9)	2.9±2.6 (72.5)
	$PM_{2.5}$	34.9±17.3	11.7±5.2 (88.0)	5.0±4.0 (57.5)	4.9±2.9 (92.5)	7.2±2.7 (75.8)	3.4±3.2 (85.0)
	PM_{10}	46.7±20.6	13.3±5.8	8.7±5.2	5.3±3.1	9.5±3.7	4±3.8
ZH	$PM_{1.0}$	12.9±4.5	6.3±2.1 (66.3)	0.3±0.3(10.3)	2.2±0.8 (71.0)	2.4±1.1 (66.7)	1.3±0.8 (76.5)
	$PM_{2.5}$	18.1±6.8	8.8±3.2 (92.6)	0.9±0.8 (31.0)	3.0±1.2 (96.8)	3.0±1.5 (83.3)	1.5±0.9 (88.2)
	PM_{10}	23.7±7.3	9.5±3.4	2.9±1.1	3.1±1.3	3.6±1.9	1.7±1.0
JFM	$PM_{1.0}$	4.4±1.6	1.8±1.0 (75.0)	0.1±0.1 (16.7)	0.5±0.3 (83.3)	1.5±0.7 (57.7)	0.3±0.2 (60.0)
	$PM_{2.5}$	5.8±2.3	2.2±1.5 (91.7)	0.2±0.1 (33.3)	0.6±0.5 (99.0)	1.8±0.8 (69.2)	0.4±0.2 (80.0)
	PM_{10}	8.0±2.6	2.4±1.5	0.6±0.3	0.6±0.5	2.6±1.1	0.5±0.3

1042   **Table 2.** Statistical parameters of samples with air masses from ocean

Site	Date	Droplet mode sulfate ($\mu g\ m^{-3}$)	Percentage of sulfate in droplet mode (%)	T (℃)	RH (%)	P (hPa)	WS (m s^{-1})	Low Cloud cover (%)
GZ	2010/5/8	7.4	61	27.5	82.0	997.1	1.9	70
	2010/5/12	11.1	65	25.0	77.5	1002.9	1.5	60
ZH	2010/5/12	9.5	67	24.9	83.0	1006.1	3.4	70
	2010/6/1	6.8	67	24.8	80.0	1002.0	5.1	70
JFM	2010/5/4	2.2	64	22.0	83.0	916.9	1.0	70
	2010/5/13	2.5	67	23.7	75.8	918.3	1.8	70

1043